Large Eddy Simulation of Rough Surface Flow in Shallow Open Channels

Zeng Zhang

A Thesis

in

The Department

of

Building, Civil, and Environmental Engineering

Presented in Partial Fulfilment of the Requirements

For the Degree of Master of Applied Science in Civil Engineering at

Concordia University

Montreal, Quebec, Canada

January 2018

CONCORDIA UNIVERSITY
School of Graduate Studies

This is to certify that the thesis prepared

By: Zeng Zhang

Entitled: Large Eddy Simulation of Rough Surface Flow in Shallow Open Channels
and submitted in partial fulfillment of the requirements for the degree of

Master of Applied Science (Civil Engineering)

complies with the regulations of the University and meets the accepted standards with respect to originality and quality.

Signed by the final examining committee:

Dr. Catherine Mulligan Chair

Dr. Georgois Vatistas Examiner

Dr. Leon Wang Examiner

Dr. S. Li Supervisor

Approved by Dr. Ashutosh Bagchi
Chair of Department or Graduate Program Director

Dr. Amir Asif
Dean of Faculty

Date March, 2018

ABSTRACT

Large Eddy Simulation of Rough Surface Flow in Shallow Open Channels

Zeng Zhang

Open channels often have a rough bed surface. A good understanding of the characteristics of water flow over the rough bed is important for many applications in hydraulic engineering. Examples include investigations of the re-suspension and transport of contaminated bed materials, channel erosion, and the effectiveness of dissipating excessive flow energy. In this thesis, the rough surface was created by placing transverse bars at a flat channel-bed in one case and cubes in the other case, and the velocity field of rough-surface flow was computed through large eddy simulations (LES). This thesis aims to evaluate suitable computing strategies, validate computational results using available experimental data, and explore the detailed structures of near-bed flow.

On the basis of the bars′ centre-to-centre spacing, λ, relative to their vertical dimension, k, studies of the rough-surface flow classify the rough elements as k-type and d-type ribs. Previous experimental studies of the rough-surface flow have produced some measurements of flow velocities, provided assessments of the suitability of existing methods for determining the shear velocity, and comparisons of characteristics between flow over d-type ribs and that over smooth walls, as well as between flow over ribs and that over transverse rows of staggered cubes. The main findings were that similarities existed in the outer layer between flow over three-dimensional roughness and flow over smooth walls. Some previous numerical studies introduced a form-drag term in the momentum equation to indirectly allow for the effect of roughness on the flow. Other numerical studies used obstacles as bed roughness elements, and applied non-slip conditions at their surfaces. A significant limitation of the previous studies is the use of conditions of fully developed boundary layer flow with zero-pressure gradient. This would be very approximate for water flows in shallow open channels. The canonical turbulent boundary layers are not expected to be valid, because the boundary layer thickness is a significant fraction of the depth of flow. Further investigations of the flow characteristics are needed.

The large eddy simulations reported in this thesis capture the flow characteristics in the near-bed

region. They gave numerical predictions of the flow field over transverse bars in shallow open channels at a range of λ/k ratios. The predictions provide accurate horizontal turbulence intensities, and horizontal velocity. It seems that large eddy simulations produce accurate flow characteristics in the streamwise direction, but less accurate results in the vertical direction. A plausible reason is the side wall effects. It is challenging to realistically capture secondary flow that creates transverse vortices in the transverse direction on both sides of the channel. These vortices cause upward motions at the middle of the channel.

The power spectrum density (PSD) curves for all the runs show characteristics of energy cascade that are consistent with the results reported in the literature (Rodi, 2017), in particular the energy distribution for the inertia subrange.

It has been concluded that: 1) an increase in the λ/k ratio leads to a decrease in the region of reverse flow within the cavity, and an increase in the shear stress on the upstream face of transverse bars; 2) in the case of flow over staggered cubes, they tend to restrict reverse flow, and cause the shear stress at the upstream edge of the cubes to increase; 3) it is suitable to apply cyclic boundary conditions in both the transverse and streamwise directions in simulations of fully developed flow.

Table of Contents

List of Symbols

The following symbols have been used in this thesis.

Roman Character

A	Area (m^2)
C	Chezy coefficient
C_s	Smagorinsky constant
C_o	Courant number
C_f	Skin friction coefficient
C_D	Drag coefficient
D	Domain where the integration of filter function (G) perform
D_{50}	Cumulative 50% point of diameter (or 50% pass particle size) (m)
d	Pipe diameter (m)
E( )	Energy spectrum function
F{ }	Fourier transform
f	Friction factor
f	Un-filtered local quantity
$\overline{f}$	Resolved scale component of the un-filtered local quantity
f'	Sub-grid scale (SGS) component of un-filtered the local quantity
G	Filter function
g_i	Gravitational acceleration in tensor notation (m/s^2)
H	Water depth (m)
I_i	Dimensionless turbulence intensity component in x_i direction
k	Roughness height (m) or turbulence kinetic energy (m^2/s^2)
k_s	Equivalent roughness height corresponding to k
k_s^+	Equivalent roughness height in wall unit
L	Length (m)
L_{ij}	Part of the sub-test-scale stresses that are resolved between $\tilde{\_}$ and Δ (m^2/s^2)
l	Character length (m)
N	Number of records in the time series of velocity components

n	Manning coefficient
P	Pressure (Pa)
q	Velocity scale expressing sub-grid scale motion (m/s)
$R_{ij}(r)$	Two-point covariance
S_f	Friction slop
R	Hydraulic radius (m)
Re	Dimensionless Reynolds number
r (x_1, x_2, x_3)	Position of resolved quantity $\bar{f}$
r′ (x_1, x_2, x_3)	Position of local quantity f
$\overline{S_{ij}}$	Resolved rate of strain (s^{-1})
T_{ij}	Sub-test scale stresses (m^2/s^2)
t	Time (s)
U_b	Bulk velocity (m/s)
U_e	Time-averaged free stream velocity (m/s)
U_i	Time-average velocity in tensor notation (m/s)
U_τ	Frictional velocity (m/s)
u_i	Un-filtered, local velocity in tensor notation (m/s)
$\bar{u}_i$	Resolved scale velocity in tensor notation (m/s)
u_i'	Sub-grid scale (SGS) velocity in tensor notation (m/s)
$-\overline{u_i u_j}$	Reynolds shear stress (m^2/s^2)
V_i	Sample-space variables corresponding to U_i
x_i	Position coordinate in tensor notation (m)
x_i^+	Dimensionless wall distance in x_i direction

Greek Character

$\tilde{\Delta}$	Test filter width used by the dynamic sub-grid scale model (m)
Δ_i	Filter width in x_i direction (m)
Δt	Time step (s)
Δu_i	Time fluctuation of velocity in tensor notation ($\Delta u_i = u_i - U_i$) (m/s)
Δx_i+	Dimensionless cell dimension in wall unit in the x_i direction

δ	Boundary layer thickness (m)
$\delta( )$	Dirac delta function
δ_{ij}	Kronecker delta
θ	Angle of a cell (°)
κ	Karman constant or wavenumber (m^{-1})
λ	Centre-to-centre distance between two abjection bars (m)
μ	Dynamic viscosity (N s/ m^2)
ν	Kinematic viscosity (m^2/s)
ν_t	Eddy viscosity (m^2/s)
ρ	Water density (kg/m^3)
τ_{ij}	Anisotropic part of sub-grid scale stresses τ_{ij}^{SGS} (m^2/s^2)
$\widetilde{\tau_{ij}}$	τ_{ij} filtered by the test filter width $\tilde{\Delta}$ (m^2/s^2)
τ_{ij}	Sub-grid scale stresses (m^2/s^2)
τ_w	Wall shear stress (N/m^2)
$\Phi_{ij}( )$	Fourier transform of the two-point correlation

Symbols

~	Second filter used in the dynamic Smaorinsky model
< >	Mean velocity field
+	Normalisation using the viscous wall unit

List of Figures

List of Tables

Chapter 1
Introduction

1.1 Background

The flows of fluids over a solid surface, including air flows and water flows, are frequently encountered in the natural environment, engineering devices, and infrastructures. The study of the flows has important applications. One wishes to reduce the surface drag exerted by the surrounding fluids on aircrafts, ships, missiles, and to reduce the drag exerted by pipe walls on the flowing fluids in a pipe network for water supply, oil and gas transportation, and air ventilation. The study of the flows also has relevance to the functioning of heat exchange and electronic devices. In the field of hydraulic engineering, water channels often have a rough bed-surface, and a good understanding of water flows over the rough surface is critical. The flow characteristics are essential input to the predictions of bed-sediment incipient motions, channel erosion and siltation, and dissipation of excessive flow energy. The important applications of rough surface flow have motivated the current study.

The topic of rough surface flow is challenging for a number of reasons:

- The shape and size of roughness elements vary widely. Some are regularly spaced two-dimensional roughness such as transverse square bars, hemisphere bars, triangle bars, and dunes. Some are regularly spaced three-dimensional roughness such as staggered or aligned cubes, hemisphere, sphere, cones, and dunes. The others are random spaced roughness with the same dimension, or random spaced roughness with random dimensions.

- Different roughness elements produce different flow characteristics. Some researchers have used equivalent sand roughness in the characterization of fluid flows. Among the most important relationships are perhaps the universal velocity distribution (Schlichting et al., 1955, p.531), the Moody diagram (Moody, 1944), and Townsend's (1980) outer-layer similarity hypothesis.

- Even though some relationships have been established between surface roughness and flow characteristics, two-dimensional (2-D) roughness may affect turbulent boundary layers

differently from three-dimensional (3-D) roughness and smooth bed (Volino et al., 2011).

- Accurate measurements of near-bed flow parameters (e.g. shear velocity, and flow velocity in the near-bed region) are very difficult to obtain, because of equipment limitations. This has hindered the progress in understanding near-bed flow characteristics.

Computer simulations of near-bed flow are currently not adequate. The most accurate direct numerical simulations (DNS) requires huge computing resources, and therefore are not feasible for practical applications. Simulations using the Reynolds-averaged Navier-Stokes (RANS) equations are computationally efficient, but have difficulties to handle rough surface flow over complex geometry.

Under certain assumptions, earlier studies of the topic have made some progress in the understanding of rough surface flow. It is worth mentioning the well-known universal velocity distribution; the Moody diagram for pipe flows above certain Reynolds numbers, which provides the friction coefficient as a function of the relative roughness; and the outer-layer similarity hypothesis of Townsend (1980), who suggested that, at a relative high Reynolds number (exceeding 10000), "*the turbulent stresses, normalized by the wall shear stress, are universal outside of the roughness sublayer*" (Flack et al., 2005). The problem is that some of the assumptions are unrealistic. For example, it is problematic to represent actual roughness in three dimensions with two-dimensional roughness. 2-D and 3-D roughness may work in a different mechanism.

Understandably, laboratory experiments of rough surface flow are needed in order to obtain measurements of basic flow parameters, and estimates of other flow variables. However, they are expensive and time consuming to perform. For these reasons, experimental work covered only a limited range of experimental conditions, as was the case in Bagherimiyab & Lemmin (2013), Tachie & Adane (2007), Djenidi et al. (1999), and Volino et al. (2011). For example, experimental results are available only for some specific values for the pitch ratio λ/k, where λ denotes the centre-to-centre distance between adjacent bars and k denotes their vertical dimension. Besides, the estimates of flow variables may not be consistent among experiments and among analysis methods. For example, Bagherimiyab & Lemmin (2013) reported a difference of 20% in the estimates of shear velocity, using different analysis methods. In fact, it is extremely difficult to make accurate measurements of flow from the proximity of a solid rough surface. Technical difficulties can arise

from instrument limitations with respect to accuracy, precision, resolution, and sensitivity. There are also practical difficulties with respect to experimental setup.

It is worthwhile developing numerical models of rough surface flow. They should be validated using the first-hand data from laboratory experiments. Some recent progress in numerical modelling of rough surface flow has been reported in Miyake et al. (2000), Leonardi et al. (2007), and Coceal et al. (2007). The levels of modelling sophistication range from the incorporation of roughness-induced form drag into the momentum equations to DNS with roughness as non-slip obstacles. Almost all the existing models centred on the notion that there was a fully developed bottom boundary layer under zero-pressure gradients. While this may be acceptable for rough surface flow in deep channels, it is a questionable for shallow channels. In the latter case, the bottom boundary layer has a thickness that is a significant fraction of the total flow depth, as reported in Tachie and Adane (2007).

To the best of our knowledge, the topic of rough surface flow in shallow channels has not been investigated thoroughly. This is in spite of the research efforts made in the past. This thesis proposes to perform large eddy simulation (LES) of the flow field. LES is considered as a modification of DNS, offering the hope of accurately capturing flow details in the near-bed region, at much lower requirement of computing resources. This thesis extends experimental results of rough surface flows over regular-spaced transverse bars with different pitch ratios.

1.2 Objectives

LES is an advanced computational technique that avoids taking time averaging of the governing momentum and mass conservation equations, which is a limitation of the widely-used Reynolds-averaged modelling approach. This technique has the potential to capture detailed structures of fluid flows. Using this technique, the current study focuses on simulations of rough-surface flow in shallow open channels. The rough surface is to be created by placing transverse square bars in one case and by placing cubes in another case at the flat bed of water channels.

The specific objectives are to:

1. Establish suitable model domain setup, mesh configuration, and boundary conditions for simulations of rough surface flow, and validate the simulation results using available experimental data.

2. Investigate the dependence of flow characteristics on roughness parameters, mainly the pitch ratio (or the ratio of the centre-to-centre distance, in the streamwise direction, between adjacent bars to the roughness height), and the percentage of channel-bed area covered by the cubes.

3. Analyse and interpret the characteristics of near-bed flow, including velocity profiles, streamlines, turbulence kinetic energy, and power spectral density. These quantities are of important applications in hydraulic engineering, but are technically difficult and expensive to measure from the near-bed region of an experimental channel.

1.3 Organization of Thesis

With the objectives mentioned in the preceding section, the remaining part of this thesis is organised as follows:

The next section of this chapter provides highlights of the significant research contributions from this study.

Chapter Two gives a review of the previous studies of rough surface flow. These studies are divided into three categories on the basis of investigation approaches that the researchers used: 1) theoretical analyses, 2) experimental work, and 3) numerical simulations. The standard textbooks of hydraulics, computational fluid dynamics, and turbulence provide a compilation of the theoretical analyses, mostly published in the 1970s or earlier. The experimental work and numerical simulations reviewed in this thesis are the representative studies of rough surface flow. Almost all of the investigations involved bars or cubes in open-channel flows were from the last two decades. Various ways of creating roughness reported in the preexisting literature are reviewed in this chapter.

Chapter Three discusses the methodologies used in this thesis. The discussions include details

about the computational process of LES, the sub-grid scale (SGS) model used to compute Smagorinsky eddy viscosity and constant (C_s), and the solution algorithm. This chapter also describes the geometry, boundary conditions, mesh configurations, wall distance, and mesh independency tests.

Chapter Four presents the LES results, along with comparison of the results with available experimental data. The comparisons cover velocity profiles, turbulence intensity, and Reynolds shear stress. This chapter also discusses the characteristics of near-bed flow such as velocity distribution, turbulence kinetic energy, and power spectral density.

Chapter Five gives a summary of the key findings from this study and well as some suggestions for future research of rough surface flow.

Chapter 2
Literature Review

2.1 General Description of Rough Surface Flow

The topic of rough surface flow has received a greater level of research attention from earlier researchers. Schlichting et al. (1955, p.528) introduced a standard roughness to describe the effect of roughness on flow. The author regarded roughness (characterized by the roughness height k) as a surface covered with a dense layer of spheres with the same diameter (e.g. the sandpaper with certain roughness). The diameter of the equivalent spheres is called the equivalent sand roughness height, k_s, (Schlichting et al., 1955, p.528). Any roughness element can be generally assigned to an equivalent sand roughness. Roughness elements having the same equivalent sand roughness are considered as having the same effect.

The author derived the universal velocity distribution: $u_1^+=f(x_2^+, k_s^+)$, where x_2 denotes the vertical coordinate pointing upward from the channel-bed, u_1 denotes the along-channel velocity. + denotes the normalisation using the viscous wall unit. The details are as follows (Schlichting et al., 1955, p.525).

$$\lim_{y^+\to\infty} u_1^+(x_2^+) = \frac{1}{\kappa}\ln x_2^+ + \frac{1}{\kappa}\ln k_s^+ + f(k_s^+) \qquad [2\text{-}1]$$

where $x_2^+ = \frac{x_2}{\nu/U_\tau}; x_1^+ = \frac{x_1}{\nu/U_\tau}; k_s^+ = \frac{k_s}{\nu/U_\tau};$

κ is the Karman constant (equal to 0.41);

U_τ is the friction velocity;

ν is the kinematic viscosity.

$\lim_{k_s^+\to 0} f(k_s^+) = 5.0$ (hydraulically smooth, $k_s^+ < 5$),

$\lim_{k_s^+\to\infty} [\frac{1}{\kappa}\ln k_s^+ + f(k_s^+)] = 8.0$ (fully rough, $k_s^+ > 70$)

The author further conducted an experiment of turbulence flow over ribs with different roughness height. The relationship between velocity distributions and k_s^+ is shown in Figure 2-1.

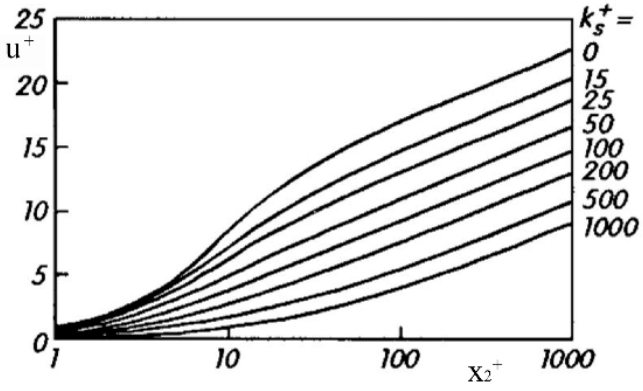

Figure 2-1 Universal velocity distribution $u^+ = f(x_2^+, ks^+)$ (Schlichting et al., 1955, p.531)

No.	Type	Dimension	D [cm]	d [cm]	k [cm]	k_S [cm]	Photo
1	Spheres		4	0.41	0.41	0.093	
2			2	0.41	0.41	0.344	
3			1	0.41	0.41	1.26	
4			0.6	0.41	0.41	1.56	
5			Tightest packing	0.41	0.41	0.257	
6			1	0.21	0.21	0.172	
7			0.5	0.21	0.21	0.759	
8	Hemispherical caps		4	0.8	0.26	0.031	
9			3	0.8	0.26	0.049	
10			2	0.8	0.26	0.149	
11			Tightest packing	0.8	0.26	0.365	
12	Cones		4	0.8	0.375	0.059	
13			3	0.8	0.375	0.164	
14			2	0.8	0.375	0.374	
15	"Short" angles		4	0.8	0.30	0.291	
16			3	0.8	0.30	0.618	
17			2	0.8	0.30	1.47	

Figure 2-2 Results from roughness measurements on regularly placed roughness elements

(Schlichting et al., 1955, p.533).

Schlichting et al. (1955) further determined the equivalent sand roughness for a variety of regularly arranged roughness elements with different densities. Elements include spheres, cons, hemispherical caps, and shot angles, as shown in Figure 2-2.

The universal velocity distribution, along with the equivalent sand roughness, is a powerful combination. The roughness element height can be transformed to the equivalent sand roughness, and further investigated by using the universal velocity distribution. The mean velocity profiles on the universal velocity distribution provide useful information such as bed shear stress.

As an alternative to determining the equivalent roughness height and universal velocity distribution, some researchers allow for the effects of roughness elements by applying the resultant drag forces on the rough surface. A drag force can be divided into skin friction drag and form (pressure) drag. The former is due to the viscous shear at the interface between solid boundaries and fluid. The latter is due to the combination of positive pressure on the front and negative pressure on the back of obstacles. Obstacles or wall boundaries in fluids may have one or both of the drags.

The drag force is calculated by:

$$F_D = \frac{1}{2}\rho C_D A u_1^2 \qquad [2\text{-}2]$$

where ρ is the mass density of fluids, C_D is the drag coefficient, A is the reference area. C_D is not a constant but varies as a function of flow speed, flow direction, object position, object size, fluid density and fluid viscosity. The drag coefficient in drag force equation works in a similar manner as the friction factor, f, in the Darcy-Weisbach, Chezy coefficient, C, in the Chezy equation, and Manning coefficient, n, in Manning equation (Akan, 2011, p.70-73).

$$\text{Darcy-Weisbach: } S_f = \frac{f}{R}\frac{u_1^2}{8g} \qquad [2\text{-}3]$$

$$\text{Chezy: } S_f = u_1^2 C^2 / R \qquad [2\text{-}4]$$

$$\text{Manning: } S_f = u_1^2 n^2 / R^{4/3} \qquad [2\text{-}5]$$

where S_f is friction slope, meaning the boundary friction force per unit weight of water present in channels, and R is the hydraulic radius. The Darcy-Weisbach equation (Equation [2-3]) and the Moody diagram express the friction factor, f, as a function of the Reynolds number (Re) and roughness height (k).

Chow (1959) conceptually classified flows over rough bed surfaces into three basic types: 1) isolated-roughness flow, 2) wake-interference flow, and 3) quasi-smooth flow. The first type of flow features wake and vortex at each rough element being completely developed and dissipated before the next element is reached. The second type of flow exhibits intense and complex vorticity, and turbulent mixing, as a result of the interference of the wake and vortex at each rough element with those developed at the following rough element. The third type of flow virtually skims the top of the rough elements, with stable eddies in the cavities between the elements. These classifications are useful but do not any quantitative description of the flow structures.

Perry et al. (1969) discussed the special case of flow over periodic, repeated transverse square bars as roughness elements. The author classified the elements into two types: k-type, and d-type. The former means that the roughness height, k, is the significant length scale that determines flow characters, whereas the latter means that the boundary layer thickness is the major factor of determination of flow characteristics. The pitch ratio $\lambda / k \leq 4$ is usually characterized as d-type roughness, and $\lambda/k > 4$ as k-type roughness (Tachie & Adane, 2007), where λ is the spacing distance between abjection roughness elements; k is the roughness height (Figure 2-3). Leonardi et al. (2007) suggested that it is difficult to precisely determine the demarcation between the two types of roughness. This is because an accurate measurement of flow near the wall is difficult to make, particularly the measurements of the friction velocity or equivalently the bed shear stress.

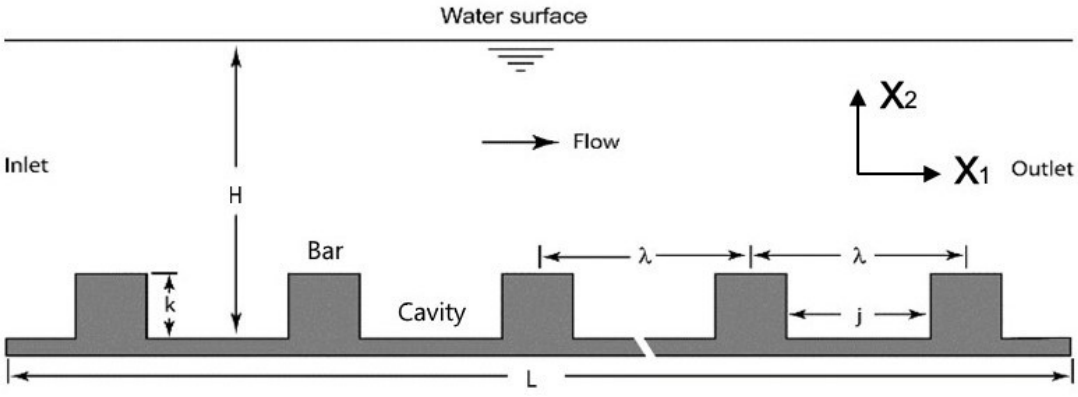

Figure 2-3 Side view of the rough channel with repeated transverse bars mounted on channel beds

2.2 Experimental Work

The characteristics of rough surface flow include velocity profiles, velocity fields, shear velocities, Reynolds shear stresses, turbulence intensities, momentum fluxes, eddy viscosities, and mixing lengths. Some variables are fundamental and have important engineering applications. Some of the important parameters are bed shear stress and its related Reynolds shear stress. Bed shear stress determines the hydrodynamic forces applied to sediment. Hydrodynamic force is a critical parameter for estimating the critical erosion and deposition thresholds (Bagherimiyab & Lemmin, 2013). However, some parameters are difficult to achieve. One reason is due to limitations of measurement equipment. Currently available equipment for velocity measurements has difficulties to accurately measure velocity very close to the bed. Due to this limitation, shear stress is hard to be measured directly (Bagherimiyab & Lemmin, 2013). Another reason is the limitation of the methods used for calculating parameters. For example, the spectral method estimates bed shear stress by using vertical turbulence kinetic energy. It is inaccurate because the turbulence kinetic energies in shear layers change significantly over a short vertical distance (Bagherimiyab & Lemmin, 2013). Due to the importance of flow parameters, and the difficulty of accurately measuring them, a variety of experimental equipment and methods have been applied for flow characteristic measurement or estimation.

Many experimental work of flow over rough surface have been done in wind tunnel. Raupach et al. (1980) conducted a cross-wire anemometry measurement of flow over five regular spaced cylinders. The cylinders are 6 mm in both height and diameter. The characteristics of horizontal and vertical velocity profiles were investigated. Cheng et al. (2007) conducted an x-wire anemometry measurement of flow over urban style surfaces with two different area densities. Direct measurements of surface drag were made. The wooden staggered cubes have the dimension of 20 mm. The study found that the shear stress (determined from the vertical profile of Reynolds shear stress) is under-predicted by 25% compared with the direct measurements of surface drag.

2.2.1 Acoustic Doppler Velocity (ADV) Measurement

Lacey & Rennie (2011) investigated turbulence wake characteristics induced by an isolated cube at the channel-bed. The experiment was conducted in an open channel flume with a width of 1.5 m. The flow depths of three experimental runs are 0.3, 0.25, and 0.2 m. A cube of 0.2 m (width) x 0.2 m (length) x 0.1 m (height) was mounted at the channel-bed. The Reynolds numbers (based on mean velocity and flow depth) varied from Re = 92,000 to 140,000. Three acoustic Doppler velocimeters (ADVs) were used to measure flow velocity in three directions. The upstream velocity profiles and gradients were carefully adjusted to ensure they are similar between experimental runs. This procedure isolated the effect of flow depth on wake characteristics around the cube. The study shows that the changes in relative depth have a significant effect on the flow structures in the wake of isolated obstacles.

Bagherimiyab & Lemmin (2013) measured shear velocity for smooth bed flow and for turbulent flow over a rough bed. The rough bed consists of coarse gravel (D_{50} = 1.5 cm). Acoustic Doppler velocity profile (ADVP) measurements were used in the experiments to generate full depth velocity profiles in three directions. The results from five shear velocity estimation methods were compared (the logarithmic mean velocity, the Reynolds stress, the spectral, the turbulent kinetic energy, and the wall similarity methods). All of the five methods agree very well, the maximum variant is less than 20%. No systematic trend between methods was observed. Estimations obtained from the turbulent kinetic energy and Reynolds stress methods show the best agreement among all methods. The results from the wall similarity method fall within 10% variability compared with those from

the turbulent kinetic energy and the Reynolds stress methods. Through their study, the authors confirm "*the importance of detailed velocity profile measurements for the determination of shear velocity in rough-bed flows*" (Bagherimiyab & Lemmin, 2013).

2.2.2 Particle Image Velocimetry (PIV) Measurement

Most of the prior experimental and numerical studies of transverse ribs were performed in fully developed channels and zero-pressure-gradient turbulent boundary layers (Tachie & Adane, 2007). The characteristics of transverse ribs in shallow open channel flow were less frequently studied (Tachie & Adane, 2007). Tachie & Adane (2007) measured flow characteristics of shallow open channel flow over d-type and k-type transverse ribs. The ribs have different cross-section shapes: square, circular, and semi-circular. PIV was used in this experiment to achieve instantaneous velocity in two directions (vertical and along channel directions). The spacing between corresponding points on adjacent ribs was λ =12 mm for d-type ribs ($\lambda/k = 2$) and λ = 48 mm for k-type ribs ($\lambda/k = 8$). The average height of the ribs or diameter of the circular ribs was k = 6 mm. The water depth in the channel was 75 mm. The authors found that vertical velocity profiles, horizontal velocity profiles, Reynolds stresses and mixing length distributions are independent of rib cross section for d-type. The values of skin friction coefficient for k-type ribs are significantly higher than for d-type ribs.

2.2.3 Laser Doppler Velocimetry (LDV) Measurement

Djenidi et al. (1999) compared the flow characteristics of flow over d-type transverse ribs and corresponding smooth wall results. LDV was used in this experiment to collect three-dimensional instantaneous velocities. Experiments were conducted in a closed-circuit constant-head vertical water tunnel. The spacing between corresponding points on adjacent ribs was λ =10 mm. The eight of the ribs was k = 5 mm. The water depth in the channel was 250 mm. The authors investigated the effects of the rough surface on flow characteristics. The authors found that compared to the results obtained from smooth beds, rough surface flows showed a significant increase in terms of the maximum Reynolds shear stress. The author also found smaller streamwise variations of the

local skin friction coefficient. Outflows from cavities occurred simultaneously with inflow into cavities in the rough surface flow. The authors claimed that the effects of the d-type roughness were not solely limited to the inner region of the layer but were spread out in the outer part.

Raupach et al. (1991) proposed a hypothesis claiming that outside the roughness sublayer, and provided the Reynolds number was large enough, the turbulent motion should be independent of the wall roughness. This hypothesis is also called outer-layer similarity hypothesis. However, this hypothesis may not be true. It has been a widespread concern that 2-D roughness affects turbulent boundary layers differently than 3-D roughness and smooth bed (Volino et al., 2011). Volino et al. (2011) compared flow characteristics between transverse rows of staggered cubes and square transverse bars with two types of thickness. LDV was used in this experiment to achieve three-dimensional instantaneous velocity. The experiment was conducted in a closed-circuit constant-head vertical water tunnel. For small 2D transverse bars, the spacing between corresponding points on adjacent ribs was $\lambda = 1.84$ mm ($\lambda/k = 8$); the eight of the ribs was $k = 0.23$ mm. For large 2D transverse bars $\lambda = 13.6$ mm, $k = 1.7$ mm ($\lambda/k = 8$). For rows of staggered cubes, $\lambda = 13.6$ mm, $k = 1.7$ mm ($\lambda/k = 8$). The water depth in the channel was 100 mm. The study showed outer-layer similarities between flow over three-dimensional roughness and smooth walls. Over large and small two-dimensional transverse bars, the flow conditions deviate from the outer-layer similarities. The second founding is not consistent with the results obtained by Schlichting et al. (1955 p.531), which show good outer-layer similarities among flows over bars with different pitch ratios.

Table 2-1 presents a summary of the experiments of rough surface flow. Except for the experiment conducted by Tachie & Adane (2007), none of the other experiments dealt with shallow open channel flows. Rough surface flows in shallow open channels are poorly understood.

Table 2-1 Summary of the experiments investigated rough surface flow

Reference	Experiment equipment	Roughness type	Roughness height (mm)	Flow depth (m)	Velocity measurement
Raupach et al. (1980)	wind tunnel	regular spaced cylinders	6	1.22	cross-wire anemometry
Cheng et al. (2007)	wind tunnel	staggered cubes	20	0.6	x-wire anemometry
Lacey & Rennie (2011)	open channel flume	an isolated cube	0.1	0.3, 0.25, and 0.2	ADVs
Bagherimiyab & Lemmin (2013)	open channel flume	coarse gravel	D_{50} = 15	0.19 and 0.2	ADVP
Tachie & Adane (2007)	open channel flume	regular placed transverse square bars	6	0.075	PIV
Djenidi et al. (1999)	water tunnel	regular placed transverse square bars	5	0.25	LDV
Volino et al. (2011)	water tunnel	cubes and square transverse bars	1.7	0.1	LDV

2.3 Numerical Simulation

2.3.1 Large Eddy Simulation

The correlation between the roughness height and the roughness function is unclear. The downward shift in the semi-logarithmic portion of the law of the wall" (Cui et al., 2003) couldn't be linked directly to roughness parameters. Cui et al. (2003) conducted an LES to investigate turbulence flow over transverse square bars with pitch ratios of 2, 5, and 10. The computational domain was similar to a wind tunnel with the dimensions of 2H x H x H (length x height x width). No-slip boundary conditions were applied at the top and bottom tunnel boundaries. Periodic boundary conditions were imposed in both the streamwise direction and span-wise directions. The viscosity was taken as $5 \times 10^{-5}\ U_b H$, where U_b is the bulk velocity and H is the channel height. The imposed pressure gradient was selected to maintain the Reynolds number [Re, based on the bulk velocity (U_b) and half-channel height (H/2)] at 10,000. The first grid point near the wall was located at $x_3^+ = 1$. The grid points in the near-bed region were gradually stretched out based on the first grid point, while in streamwise and spanwise directions, the grid was uniformly distributed. The LES results agree with the laboratory observations of Djenidi et al. (1999) and Okamoto et al. (1993). The mean

streamwise velocity profiles for d-type roughness agree with the experimental data. The mean streamwise velocity profiles of intermediate roughness showed slight deviations from the experimental data. The k-type roughness computational result shows under-prediction. The simulation showed shortcoming in kinetic energy prediction.

Except for the LES of staggered cubes, aligned cubes, and regular-spaced bars, elements with different cross-section shapes have been simulated previously. Xie et al. (2014) simulated two-dimensional dunes in open channel flows. The effect of water surface treatment on flow characteristics was investigated. The volume of fluid method (VOF) and rigid lid approximation (free-slip boundary condition) were applied on water surface separately. The dune has the height (H) of 0.02 m and wavelength (L) of 0.4 m. The computational domain has dimensions of 20 H (along-channel direction) x 6H (vertical direction) x 8H (cross-channel direction). A uniform grid of 240 x 144 x 96 points is discretized in the three directions, respectively. The minimum filter width in wall units was $\Delta x_1^+ = 45$ (along-channel direction), $\Delta x_3^+ = 45$ (cross-channel direction), and $\Delta x_2^+ = 1$ (vertical direction). $\Delta x_2^+ = 1$ in the near-bed region was achieved by applying the cut-cell method. Cyclic boundary conditions were imposed in both along-channel and cross-channel directions. Non-slip boundary condition was imposed on the channel bed. The study found that the predicted mean flow velocities were similar between the VOF method and rigid lid approximation. For the streamwise and vertical turbulence intensities and the Reynolds stresses, very slight discrepancies were seen between two methods in the region below the water surface. For the predicted results in the water surface region, relative large discrepancies were shown between two methods. However, such deviations do not affect the similarity of the results in the region below the water surface.

Compared with the experiments and computer simulations in the field of hydraulic engineeirng, more studies have been conducted in the field of aerodynamics. Coceal et al. (2007) numerically investigated the structure of turbulent flow over regular arrays of cubical obstacles, using large eddy simulation. The computational domain had streamwise, lateral and vertical dimensions of 16k, 12k, and 8k respectively, where k is the cube height. The space between cubes was the same as k. The Reynolds number of the flow, based on the velocity at the top of the domain and the cube height, was Re = 5800. The roughness Reynolds number is $Re_\tau = \frac{u_\tau h}{v} = 500$. A free-slip boundary condition was applied at the top of the domain. No-slip was imposed at the bottom wall and on all

the cube surfaces. Cyclic boundary condition was used in the streamwise and lateral boundaries. The LES simulation results were compared with the wind-tunnel experiments conducted by Cheng et al. (2007) and Coceal et al. (2007). The wind tunnel measurements were made over an extensive array of cubs of height h = 20 mm, with Reynolds numbers as 12000 (based on free-stream velocity and the cube height). The comparison showed very good agreement in the buffer and part of the log region.

Dritselis (2014) conducted large eddy simulation of flow over two-dimensional transverse roughness elements. The dimensions of the channel in the streamwise, wall-normal, and spanwise directions were 8h, 2h and πh, where *h* was the half of the distance between the upper wall and the top of the roughness. The roughness height of the square bars was $k = 0.2h$. The flow was confined between two non-slip walls: an upper wall, and a lower wall. The shapes of the roughness included square, circular and triangular. The roughness arrangement of λ/k = 0, 1, 3 and 7 were tested separately. All the four scenarios were performed at the same Reynolds number of $\mathrm{Re}\left(=\frac{U_b H}{\nu}\right)=5600$, where U_b is the bulk velocity, and H (equal to 2h) is the distance between upper wall and the top of the roughness. The mesh quantity in the streamwise, vertical, spanwise directions were 201, 94, and 65, respectively. A variety of subgrade-scale turbulence models were tested, including the standard dynamic Smagorinsky model, Lagrangian dynamic Smagorinsky model, and coherent structure model. The streamwise mean velocity profile, skin friction drag showed good agreement with DNS result. However, the simulation generally under-predicted the turbulence kinetic energy.

2.3.2 Direct Numerical Simulation (DNS)

Leonardi et al. (2007) conducted DNS of turbulence flow over d-type and k-type roughness with λ/k = 2, 2.5, 4, 8, 10, and 60. The Reynolds numbers (based on bulk velocity and channel half height) were equal to 2800, 7000, and 12000. The dependence of the roughness function on the Reynolds number was discussed to distinguish d-type and k-type behaviours. The authors claimed that the important difference between d-type and k-type roughness was related to the relative magnitudes of the frictional and pressure drags.

2.3.3 Roughness Element Model

Roughness can be modeled by roughness elements models. In the roughness elements model, roughness, including transverse square bars, an array of cubes, are considered by introducing a form drag term to the momentum equations. The basic concept is that the major effect of roughness elements on flow is to generate profile drag (Miyake et al., 2000). Roughness element models facilitate the computing speed by simplifying the roughness elements on the channel beds (Miyake et al., 2000).

In order to exam the effect of roughness on both boundary layers and outer regions, Miyake et al. (2000) conducted a two-dimensional DNS of turbulent flow over an array of cones. The cones had a mean height of 25 in wall units ($x_2^+ = x_2 u_\tau / v$), and the standard deviation of 5. The roughness elements have no volume, meaning that the blockage effect is neglected. The dominations of the computing domain are $2\pi H$ x $2H$ x πH (length x width x height). A non-slip boundary was applied on the upper wall. The roughness modeled by the sand-grain type roughness element model is placed on the lower wall. Periodic boundary conditions are imposed on the streamwise and spanwise directions. Two cases of roughness density are considered. The dense case has cones at all grids on the lower wall. The spare case has cones at every two grids in the streamwise direction and every four grids in the spanwise direction. The model results agree with experimental observations. The results confirm the hypothesis proposed by Raupach et al. (1991).

Table 2-2 presents a summary of the numerical simulations of rough surface flows. None of the numerical simulations dealt with rough surface flows in shallow open channels.

Table 2-2 Summary of the numerical simulations investigated rough surface flow

Reference	Simulation method	Roughness type	Boundary conditions		
			Side walls	Top boundary	Bottom boundary
Cui et al. (2003)	LES	transverse square bars	cyclic	no-slip	no-slip
Xie et al. (2014)	LES and VOF	two-dimensional dunes	cyclic	free-slip	no-slip
Coceal et al. (2007)	LES	regular arrays of cubical obstacles	cyclic	no-slip	no-slip
Dritselis (2014)	LES	transverse square bars	cyclic	no-slip	no-slip
Leonardi et al. (2007)	DNS	transverse square bars	cyclic	no-slip	no-slip
Miyake et al. (2000)	DNS and roughness element model method	cones	cyclic	no-slip	no-slip

2.4 Summary

This chapter has given a review of the current knowledge of rough surface flow:

- the universal velocity distribution, proposed by Schlichting et al. (1955);
- the dependence of the friction coefficient solely on relative roughness, from the Moody diagram for the pipe flows above the certain Reynolds numbers;
- the outer-layer similarity hypothesis, proposed by Townsend (1980);
- differences in mechanism at which the roughness of two dimensional (transverse bars) and three dimensional (e.g. cubes) works, as discussed in Volino et al., 2011);
- the importance of shear velocity as a parameter to understanding boundary layers, and five different methods for estimates of shear velocity, as summarised in Bagherimiyab & Lemmin (2013);
- flow characteristics, revealed by PIV measurements of flow over k-type and d-type ribs (Tachie & Adane 2007);
- differences of characteristics between flows over d-type transverse ribs and a smooth wall

(Djenidi et al., 1999);

- differences and similarities of characteristics between flows over transverse rows of staggered cubes and square transverse bars (Volino et al., 2011);
- representation of roughness in rough surface flow models of different levels of sophistication (Miyake et al. 2000; Leonardi et al. 2007; Coceal et al. 2007).

Chapter 3
Methodologies

3.1 Model Equations

Large eddy simulations conducted in this research use the commercial software ANSYS Fluent. The motions of fluid are governed by partial differential equations describing mass conservation and momentum balance, known as the Navier-Stokes (N-S) equations. For incompressible fluids, the equations can be written as (Rodi et al., 2013, p.13):

Continuity equation:
$$\frac{\partial u_i}{\partial x_i} = 0 \qquad [3\text{-}1]$$

Momentum equation:
$$\rho \frac{\partial u_j}{\partial t} + \rho u_i \frac{\partial u_j}{\partial x_i} = -\frac{\partial P}{\partial x_j} + \mu \frac{\partial^2 u_j}{\partial x_i^2} + \rho g_j \qquad [3\text{-}2]$$

where u_i are the unfiltered, local velocity in tensor notation (m/s); ρ is the density of water (kg/m^3); t is time (s); x_i are rectangular Cartesian coordinates in tensor notation (m); P is the pressure (Pa); g_i is gravitational accelerations in tensor notation (m/s^2).

LES filters out motions of scales smaller than the mesh size used (or sub-grid scale motions) or separate the motions of small and large-scale eddies. LES calculates the motion of large-scale eddies by directly solving the governing time-dependent N-S equations, similar to DNS. The motion of small-scale eddies is modeled by a sub-grid scale (SGS) scheme. A local quantity, *f*, is separated into resolved scale component $\bar{f}$ and sub-grid scale (SGS) component:

$$f = \bar{f} + f' \qquad [3\text{-}3]$$

The resolved quantity $\bar{f}$ is calculated in the filter method (Rodi et al., 2013, p. 17), defined by:

$$\bar{f}(r,t) = \iiint_D G(r,r',\Delta) f(r',t) dx_1 x_2 x_3 \qquad [3\text{-}4]$$

where r (x_1, x_2, x_3) is the location where the large-scale quantity $\bar{f}$ is determined; r'(x_1, x_2, x_3) is the location where the local quantity *f* is considered; D is the domain where the integration is performed; G is a filter function; Δ is the filter width of the filter function (m). The local quantity,

f, is processed by the filter function G, and integrated over the integration cell, which has the dimension of the filter width, Δ. This process produces the resolved quantity, $\bar{f}$. Some popular filter functions include: the simple volume-average box filter, the Fourier cutoff filter, and Gaussian filter. In this thesis, the finite volume discretization itself implicitly provides filtering operations, and converts the governing Navier-Stokes equations to filtered equations, where the resolvable-scale filtered velocity and pressure are the dependent variables.

Applying the filtering operation to the continuity and momentum equation leads to the filtered Navier-Stokes equations for mass conservation and momentum balance, given by (Rodi et al., 2013, p. 19):

Continuity equation:

$$\frac{\partial \overline{u_i}}{\partial x_i} = 0 \qquad [3\text{-}5]$$

Navier-Stokes equations:

$$\frac{\partial \overline{u_j}}{\partial t} + \frac{\partial \overline{u_i u_j}}{\partial x_i} = -\frac{1}{\rho}\frac{\partial \bar{P}}{\partial x_j} + \nu \frac{\partial^2 \overline{u_j}}{\partial x_i \partial x_j} + g_j \qquad [3\text{-}6]$$

where $\overline{u_i}$ denotes the resolvable-scale filtered velocity in tensor notation; ν is the kinematic viscosity. In equation [3-6], on the left-hand side, the first term expresses the rate of change of the resolved velocity; the second term is a convection term. These two terms can be interpreted as the inertial forces. On the right-hand side, the first term represents the pressure gradient; the second term is a diffusion term, associated with viscous forces; the third term is external forces applied to the fluid.

Through spatial filtering, the non-linear term $u_i u_j$ leads to the filtered quantity $\overline{u_i u_j}$ in the convection term (Equation [3-6]). $\overline{u_i u_j}$ can also be expressed as

$$\tau_{ij} = \overline{u_i u_j} - \overline{u_i}\ \overline{u_j} \qquad [3\text{-}7]$$

Substituting it into Equation [3-6] leads to:

$$\frac{\partial \overline{u_j}}{\partial t} + \frac{\partial \overline{u_i}\,\overline{u_j}}{\partial x_i} = -\frac{1}{\rho}\frac{\partial \bar{P}}{\partial x_j} + \nu \frac{\partial^2 \overline{u_j}}{\partial x_i \partial x_j} - \frac{\partial \tau_{ij}}{\partial x_i} + g_j \qquad [3\text{-}8]$$

where τ_{ij} is called sub-grid scale stresses, representing the effect of the unresolved fluctuations on the resolved motion (Rodi et al., 2013, p. 19). The sub-grid scale stresses include the Leonard stress, the cross-term stress, and the sub-grid scale Reynolds stress. They are associated with the interaction of fluctuations of larger-scale resolvable fields, the interaction of resolvable and unresolvable fluctuations, and the interaction of unresolvable fluctuations, respectively. Because the sub-grid scale stresses are non-linear, in this thesis, they are modeled by a sub-grid scale model. Some of the popular eddy viscosity models are the purely algebraic Smagorinsky model and its dynamic variant, and the WALE model.

3.1 Sub-grid Scale (SGS) Model

In this thesis, the sub-grid scale stress, τ_{ij}, is solved by the dynamic Smaorinsky model. This model splits the sub-grid scale (SGS) stresses into an isotropic and an anisotropic component (Fluent, 2013, p. 100):

$$\tau_{ij} = \underbrace{\tau_{ii} - \frac{1}{3}\tau_{kk}\delta_{ij}}_{anisotropic} + \underbrace{\frac{1}{3}\tau_{kk}\delta_{ii}}_{isotropic} \qquad [3\text{-}9]$$

where δ_{ij} is the Kronecker delta. The isotropic part of the SGS stresses is twice the kinetic energy of the SGS fluctuations (Rodi et al., 2013, p. 24). This component usually adds to the filtered pressure term (Equation [3-6]). In analogy to the similar relation in RANS, the anisotropic part is related to the small-scale modeled motion through eddy viscosity ν_t and resolved rate of strain, $\overline{S_{ij}}$:

$$\tau_{ij} - \frac{1}{3}\tau_{kk}\delta_{ij} = -2\nu_t \overline{S_{ij}} \qquad [3\text{-}10]$$

$$\overline{S_{ij}} = \frac{1}{2}\left(\frac{\partial \overline{u_i}}{\partial x_j} + \frac{\partial \overline{u_j}}{\partial x_i}\right) \quad [3\text{-}11]$$

where ν_t is calculated through dimension analysis (Rodi et al., 2013, p. 25):

$$\nu_t = lq \quad [3\text{-}12]$$

where l is a character length; q is a velocity scale expressing sub-grid scale motion. With the eddy viscosity characterising the unresolved sub-grid scale fluctuation, the character length is expressed by (Rodi et al., 2013, p. 25):

$$l = C_s \Delta \quad [3\text{-}13]$$

where C_s is an empirical constant; Δ is a filter width. This parameter is also known as the grid scale. It is an overall scale of the sub-grid scale motion, equal to $(\Delta_1\Delta_2\Delta_3)^{1/3}$ if the grid dimensions in the three coordinate directions are different. Similar to the Prandtl's mixing length theory, the velocity scale q is expressed as (Rodi et al., 2013, p. 26):

$$q = l\left|\overline{S_{ij}}\right| = C_s \Delta \left|\overline{S_{ij}}\right| \quad [3\text{-}14]$$

$$\left|\overline{S_{ij}}\right| = \sqrt{2\overline{S_{ij}}\,\overline{S_{ij}}} \quad [3\text{-}15]$$

Substitute q into $\nu_t = lq$ (Equation [3-12]) yields

$$\nu_t = lq = l^2\left|\overline{S_{ij}}\right| = (C_s\Delta)^2\left|\overline{S_{ij}}\right| \quad [3\text{-}16]$$

Substitute ν_t into Equation [3-10] gives

$$\tau_{ij} - \frac{1}{3}\tau_{kk}\delta_{ij} = -2(C_s\Delta)^2\left|\overline{S_{ij}}\right|\overline{S_{ij}} \quad [3\text{-}17]$$

In the purely algebraic Smagorinsky model, C_s is considered as constant. That means the motion in the inertial subrange is assumed as local equilibrium (Rodi et al., 2013, p. 26). Lilly (1992) suggested $C_s = 0.165$. In the viscous sublayer, this assumption leads to a high value of ν_t. It is because the large velocity gradient in this region causes a high value of strain rate $|S_{ij}|$. The result is not realistic. In the viscous sublayer, eddy viscosity ν_t should reduce to zero when approaching

a boundary.

Many modification methods have been proposed in order to achieve a realistic eddy viscosity value. In this thesis, the dynamic sub-grid scale model proposed by Germano et al. (1991) is used. This model calculates model parameters, such as C_s, based on the information from the smallest resolved scales. The authors defined a second filter, a test filter ($\tilde{\square}$), equalling to twice the filter width Δ, then applied the Germano's identity to calculate C_s.

Germano's identity:

$$L_{ij} = T_{ij} - \tilde{\tau}_{ij} \quad [3\text{-}18]$$

where the test filter is denoted by ~. The relationship among τ_{ij}, L_{ij}, and T_{ij} is illustrated in Figure 3-1 (Rodi et al., 2013, p. 28):

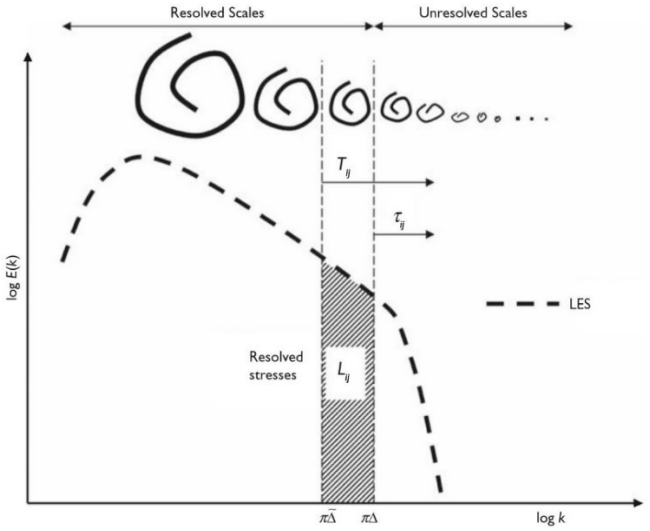

Figure 3-1 Typical energy spectrum of LES (Rodi et al., 2013, p. 28).

In Figure 3-1, k is the wave number, and E(k) is the associate energy. The sub-grid scale stress, τ_{ij}, represents the stresses resolved by the filter width Δ or the cell size used for space discretization. The sub-test scale stress, T_{ij}, represents the stress resolved by filter width, $\tilde{\square}$. L_{ij} represents the part of the sub-test-scale stress resolved between $\tilde{\square}$ and Δ (i.e. the smallest resolved scales).

$\widetilde{\tau_{ij}}$ is the anisotropic part of τ_{ij} (Equation [3-9]) filtered by the test filter width $\tilde{\Delta}$. Applying the model expressed by Equation [3-17] to calculate the anisotropic part of both T_{ij} and $\widetilde{\tau_{ij}}$ gives:

$$\widetilde{\tau_{ij}} = -2(C_S\Delta)^2 \widetilde{|\bar{S}_{ij}|\bar{S}_{ij}} \quad [3\text{-}19]$$

$$T_{ij} = -2(C_s\tilde{\Delta})^2 \left|\tilde{\bar{S}}_{ij}\right| \tilde{\bar{S}}_{ij} \quad [3\text{-}20]$$

where the double-filtered strain rate tensor is defined as:

$$\tilde{\bar{S}}_{ij} = \frac{1}{2}\left(\frac{\partial \tilde{\bar{u}}_i}{\partial x_j} + \frac{\partial \tilde{\bar{u}}_j}{\partial x_i}\right) \quad [3\text{-}21]$$

$$\left|\tilde{\bar{S}}_{ij}\right| = \sqrt{2\,\tilde{\bar{S}}_{ij}\,\tilde{\bar{S}}_{ij}} \quad [3\text{-}22]$$

Assume that C_s in T_{ij} and $\widetilde{\tau_{ij}}$ is the same. Substituting T_{ij} and $\widetilde{\tau_{ij}}$ into Germano's identity (Rodi et al., 2013) leads to

$$L_{ij} = -2(C_s\Delta)^2 M_{ij} \quad [3\text{-}23]$$

where

$$M_{ij} = \frac{\tilde{\Delta}^2}{\Delta^2}\left|\tilde{\bar{S}}_{ij}\right| \tilde{\bar{S}}_{ij} - \widetilde{|\bar{S}_{ij}|\bar{S}_{ij}} \quad [3\text{-}24]$$

C_s that best satisfies Equation [3-23] is solved from (Lilly, 1992):

$$C_s\Delta^2 = \frac{1}{2}\frac{\langle L_{ij}M_{ij}\rangle}{\langle M_{ij}M_{ij}\rangle} \quad [3\text{-}25]$$

where the angle brackets mean averaging over regions of statistical homogeneity or fluid trajectories.

3.2 Space and Time Discretization

The filtered Navier-Stokes equation [3-6] is discretized using the cell-center based finite volume method. The procedure involves dividing a computing domain into a large number of cells. The cells are non-staggered, or co-located grids, meaning that pressure and velocity components are stored at the centroid of each control volume. This is different from vortex-based (element-based) finite volume methods, for which parameters are stored at grid points. Over each cell-center based cell, the governing partial differential equations are integrated to yield algebraic equations for discrete dependent variables. Then, interpolation profiles are applied to describe the variation of variables between cell centroids. The resulting solution must satisfy the conservation of mass and momentum.

The rough surface flow is time-dependent. Thus, it is necessary to perform time discretisation of the filtered Navier-Stokes equation [3-6]. The integration of each term in the discretised equations uses a time step Δt small enough to enhance numerical accuracy. Estimates of Δt are based on the criterion that the Courant number is smaller than unity:

$$C_o = \frac{U\Delta t}{\Delta} \qquad [3\text{-}26]$$

where U denotes the time-average velocity; Δt is the time step; Δ is the filter width in the streamwise direction. For all the simulations, the maximum time-average velocity is 0.4 m/s, the smallest streamwise direction filter width, Δ, in the computing domain is 0.4 mm, and thus Δt = 0.001 s for $C_o = 1$. For all the simulations, a time step that satisfies $C_o < 1$ is used.

The time steps for Runs 1 to 6 (Table 3-1and 3-2) are 0.0005, 0.0001, 0.0001, 0.001, 0.00005, and 0.0005 s, respectively. The pitch ratio in the Table 3-1 is explained in Figure 2-3. The convergence criteria are the same. The continuity, x_1-velocity, x_2-velocity, and x_3-velocity equations have the same convergence criteria of 10^{-4}. Note that simulations with a larger time step take more iterations to satisfy the convergence criteria.

Table 3-1 Summary of the values of the parameters used for the simulations

Run ID	Pitch ratio (λ/k)	Cells	Time step (s)	Data sampling frequency (Hz)	Free stream velocity (m/s)	Note
1	2	1117857	0.001	20	0.4	d-type roughness flow
2	4	769674	0.0001	10	0.3689	
3	6	640100	0.0001	10	0.3860	
4	8	1689732	0.001	10	0.3796	k-type roughness flow
5	2	776784	0.00005	20	0.4447	3D cubes
6	8	2805000	0.001	20	0.3796	k-type roughness flow

Table 3-2 Mesh configurations used in the simulations

Run ID	Mesh size (Δx_1, Δx_2, mm)			Growth rate		cells	Time step (s)
	Bar (or cube) top	Cavity bed	Water surface	Channel bed	Upper water column		
1	(0.25-1, 0.05-0.5)	(0.5-1, 0.05-0.5)	(0.5- 2, 2.5)	1.2	1.05	1117857	0.001
2	(0.25-1, 0.05-0.5)	(0.5-1.5, 0.05-0.5)	(0.5- 2, 2.5)	1.1	1.05	769674	0.0001
3	(0.25-1, 0.05-0.5)	(0.5-2, 0.05-0.5)	(0.5- 2, 2.5)	1.1	1.05	640100	0.0001
4	(0.25-1, 0.05-0.5)	(0.5-2, 0.05-0.5)	(0.5- 2, 3.5)	1.2	1.05	1689732	0.001
5	(0.25-1, 0.05-0.5)	(0.5-1, 0.05-0.5)	(0.5- 2, 2.5)	1.2	1.05	776784	0.00005
6	(0.25, 0.05-0.5)	(0.5-1, 0.05-0.5)	(0.5-1, 3.5)	1.2	1.05	2805000	0.001

3.3 Solution Algorithms

In this thesis, a pressure-based solver is used to solve the governing equations for continuity and momentum balances. The procedure involves deriving a pressure equation from the continuity and the momentum equations by using the pressure-velocity coupling algorithm. The pressure-based solver is a segregated solver, which solves for pressure correction and momentum sequentially. By solving the pressure (or pressure correction) equation, the constraint of mass conservation

(continuity) of velocity fields is achieved. Instead of solving the continuity and momentum equations, the momentum and pressure-based continuity equations are solved.

The pressure-velocity coupling algorithm used is the Pressure-Implicit with Splitting of Operators (PISO). All discrete conservation equations (e.g. momentum) are obeyed in all cells to the tolerance of 10^{-4}. The process steps of the segregated pressure-based solver with PISO algorithm are illustrated in Figure 3-2. First, at the begin of a calculation, the initialized solutions will be assigned to fluid properties. Second, the momentum equations in x_1, x_2, x_3 directions are solved in turn (segregated from one another) to achieve the predicted velocity field. Then, the estimated pressure field is solved by substituting the predicted velocity field into the pressure equations. Next, the corrected velocity field is obtained by recalculation using the estimated pressure field. This procedure is repeated for a few times in the PISO loop until the continuity is satisfied.

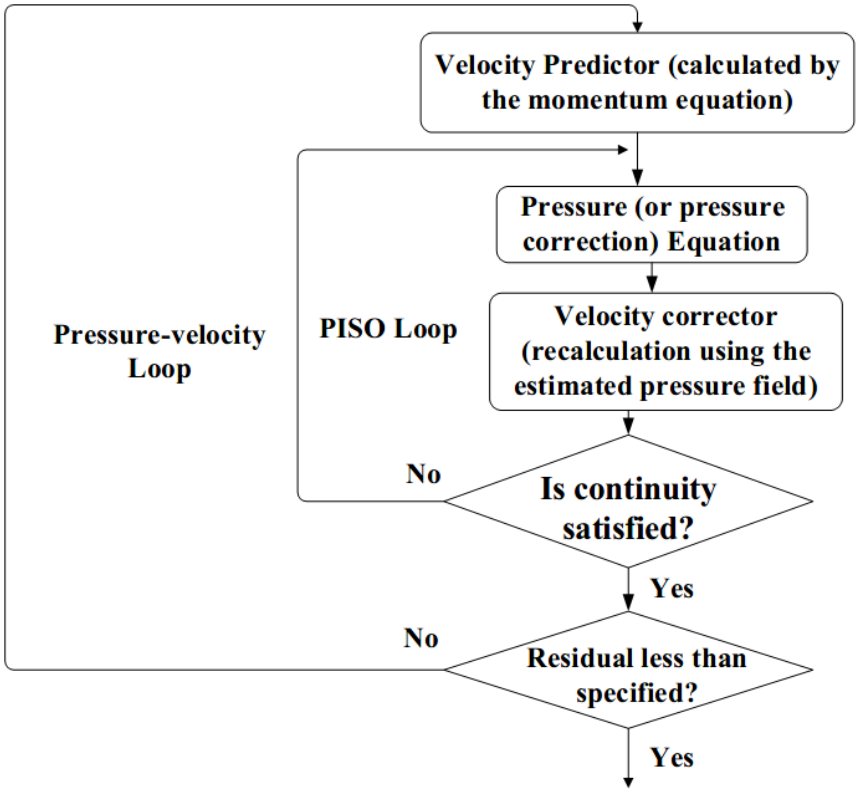

Figure 3-2 Process steps of the segregated pressure-based solver with PISO algorithm (from Giannopapa & Papadakis, 2007)

The pressure equation is solved by correcting mass fluxes, but this correction is approximate for highly skewed mesh. The skewness correction recalculates the pressure-correction solution using

a corrected mass flux. The highest normalized mesh skewness in this thesis is 0.5, as determined below:

$$\text{Normalized Equiangular Skewness} = \max\left[\frac{\theta_{\max} - \theta_e}{180° - \theta_e}, \frac{\theta_e - \theta_{\min}}{\theta_e}\right] \quad [3\text{-}27]$$

where θ_{max} is the largest angle in the cell, θ_{min} is the smallest angle in the cell, θ_e is the angle for an equiangular cell. Therefore, it is necessary to implement the skewness correction.

After the flow variables (stored at the cell centre) are solved by the pressure-based solver, they are interpolated to the faces of control volumes. The method for interpolations used in this thesis is a least square cell-based method applied to the gradient of the variables. A second order interpolation scheme is used for calculating cell-face pressures. The bounded central differencing scheme is used for interpolating the convection term.

3.4 Geometry Description and Boundary Conditions

In this thesis, six runs were performed (Tables 3-1 and 3-2). Runs 1 to 4 computed turbulent flows over transverse square bars with various pitch ratio, λ/k. The pitch ratios for Runs 1 to 4 are 2, 4, 6, and 8, respectively (Tables 3-1 and 3-2). Run 6 computed turbulent flow over 3D cubes. The cubes were staggered with a pitch ratio of 2. Run 5 ($\lambda/k = 8$) implemented the same conditions as Run 4, but used a finer mesh. Tests for mesh independency were performed by comparing simulation results between Runs 4 and 6. Run 4 was used to test mesh independency because it had the most complex flow characteristics among Runs 1 to 4. Once the mesh independency was achieved for Run 4, the results for Runs 1 to 3 with the same mesh configurations were considered to be mesh independent. A summary of all the runs is given in Tables 3-1 and 3-2.

In Figure 3-3 to 3.12, the trimetric and front view of the geometry for Runs 1 to 5 is shown. 2D transverse square bars are evenly placed at the channel-bed. These bars are 0.006, 0.006, and 0.075 m, respectively, in dimensions in the x_1- (streamwise or along-channel), x_2- (vertical), and x_3- (cross-channel) directions. The model channel has a half cavity with a width of 0.003 m in its entrance and exit, before the most upstream bar and after the most downstream bar, respectively. These two halves of cavities constitute a whole cavity to meet the requirement of cyclic boundary

conditions. The model channels for Runs 1 to 5 has a length of 0.156, 0.168, 0.18, 0.48, 0.48 m, respectively.

These lengths are more than two times the flow depth, giving a balance between computing costs and computational accuracy. A certain length may work in favour of a corresponding wave frequency. The preference is to use the largest length, within the capacity of available computing resources. The strategy used in this thesis is to minimise the possible domination of a certain wave number and include the realistic category of different wave numbers. The length of the model channel, along with the geometric complexity and mesh resolutions, affect the total number of computing nodes, and hence the computing costs. Regions near bars are covered with finer cells in order to accurately resolve flow details. The consideration of a balance between computing costs and computational accuracy leads to the selections of different lengths for the different runs.

In Figure 3-11 and Figure 3-12, the trimetric and front view of the channel for Run 5 is plotted. 3-D cubes are placed at the channel-bed with a pitch ratio of $\lambda/k = 2$. The cubes have the size of 0.006 m in all three dimensions. The channel dimensions are 0.024, 0.075, and 0.075 m, respectively in the x_1-, x_2- and x_3-directions. The channel has identical or repeated sections at all the four lateral boundaries, making it suitable to apply cyclic boundary conditions in both the streamwise and transverse directions.

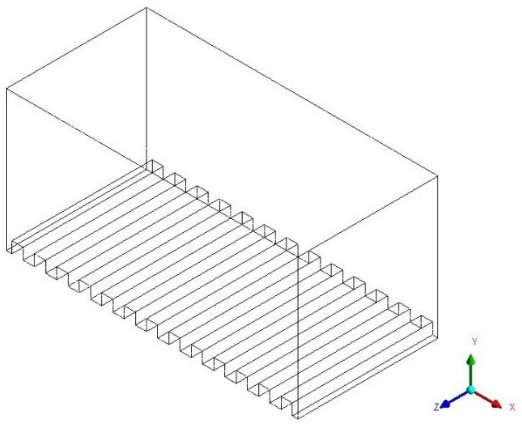

Figure 3-3 Trimetric view of the model channel for Run 1 ($\lambda/k = 2$, Tables 3-1 and 3-2). The x-axis (the red arrow, the same henceforward) points positively in the streamwise direction (x_1); the y-axis (the green arrow, the same henceforward) points positively in the vertical direction (x_2); the z-axis (the blue arrow, the same henceforward) points positively in the transverse direction

(x_3).

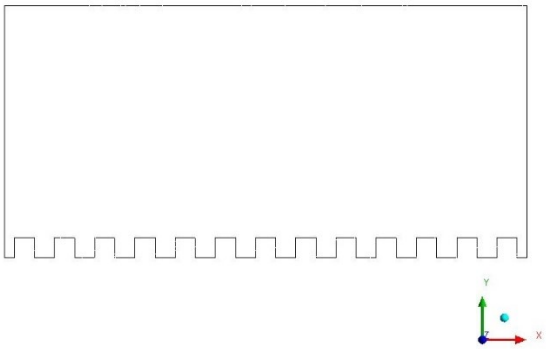

Figure 3-4 Side view of the model channel for Run 1.

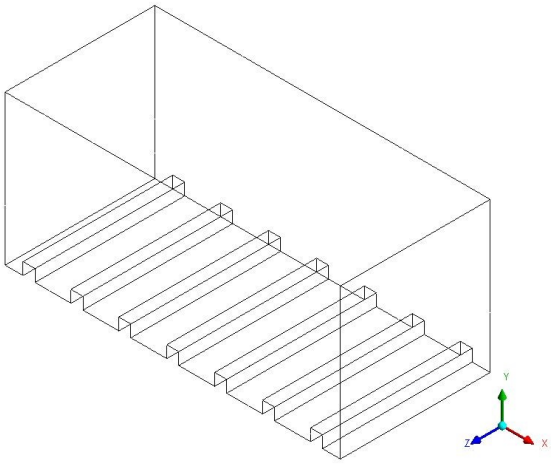

Figure 3-5 Trimetric view of the model channel for Run 2 (λ/k = 4).

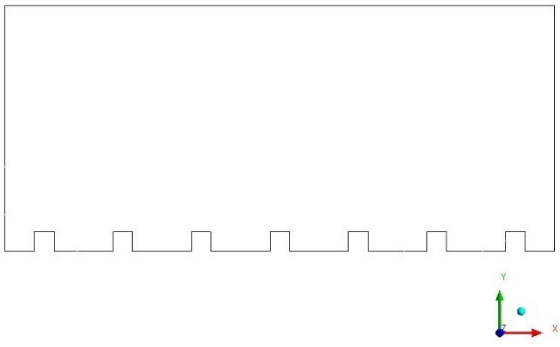

Figure 3-6 Side view of the model channel for Run 2.

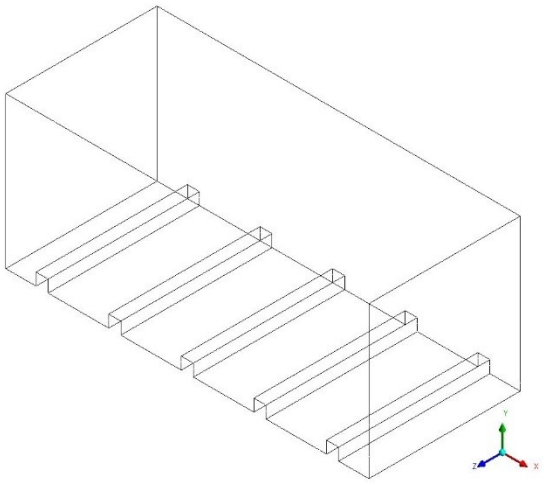

Figure 3-7 Trimetric view of the model channel for Run 3 (λ/k = 6).

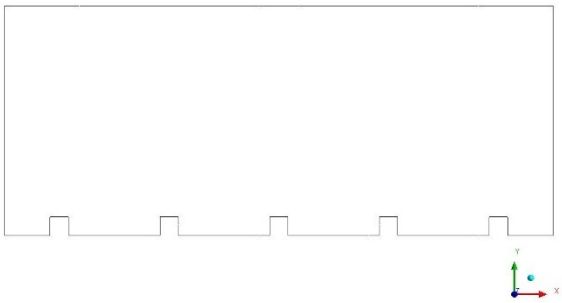

Figure 3-8 Side view of the model channel for Run 3.

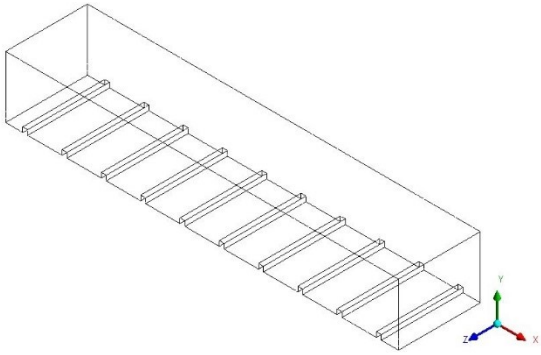

Figure 3-9 Trimetric view of the model channel for Run 4 (λ/k = 8).

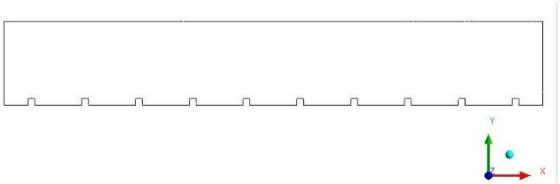

Figure 3-10 Side view of the model channel for Run 4.

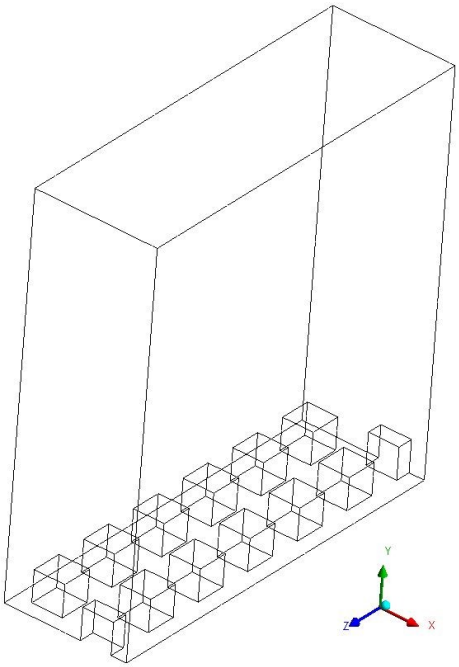

Figure 3-11 Trimetric view of the model channel for Run 5 (3-D cubes).

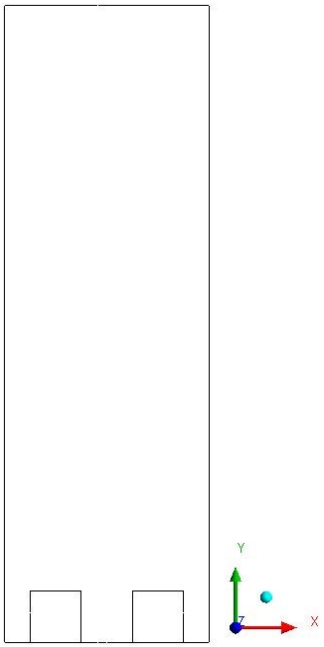

Figure 3-12 Side view of the model channel for Run 5.

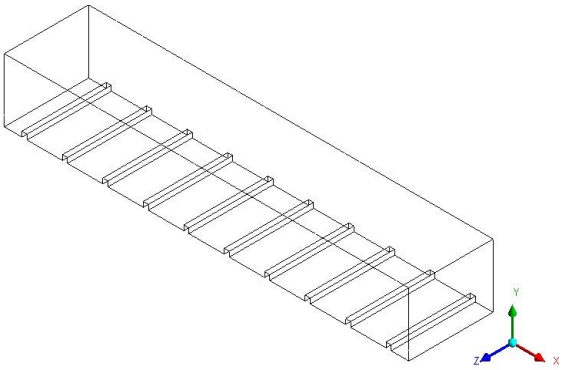

Figure 3-13 Trimetric view of the model channel for Run 6 (λ/k = 8).

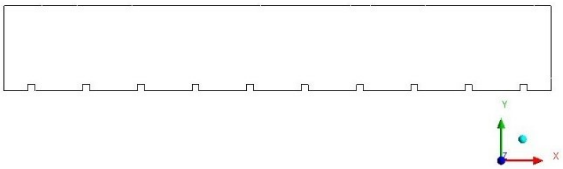

Figure 3-14 Side view of the model channel for Run 6.

At the boundaries of the model channels, conditions of flow variables are specified. These boundaries include the channel-bed, two lateral boundaries, the inlet at the upstream, the outlet at the downstream, and the water surface (Figures 3-15, 3-16, 3-17, 3-18).

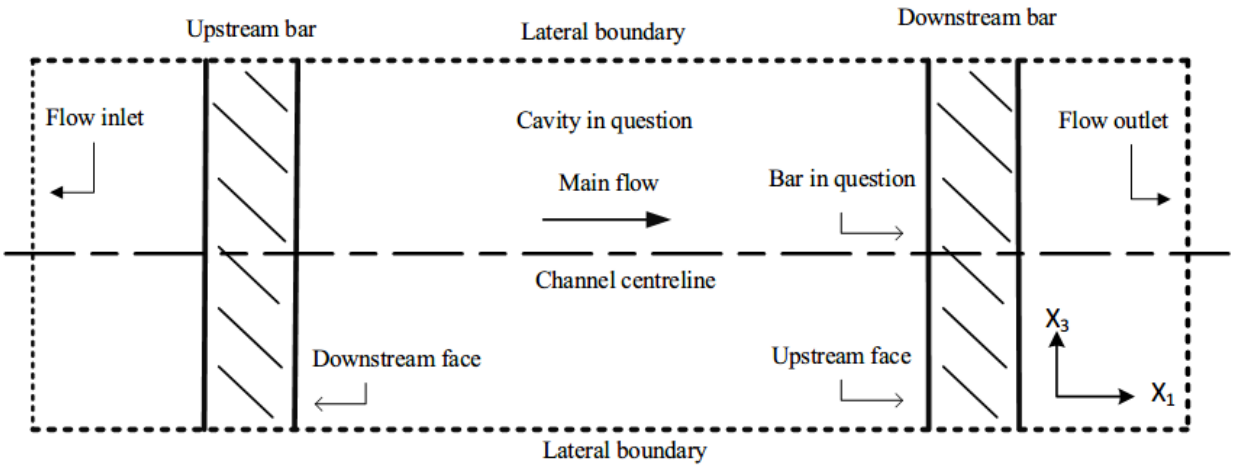

Figure 3-15 Top view of the model channels with rough elements (bars) at the bed. For clarity, only part of the model channel and two roughness elements are shown. The channel centreline is

located at x_3=0.0375 for all the runs.

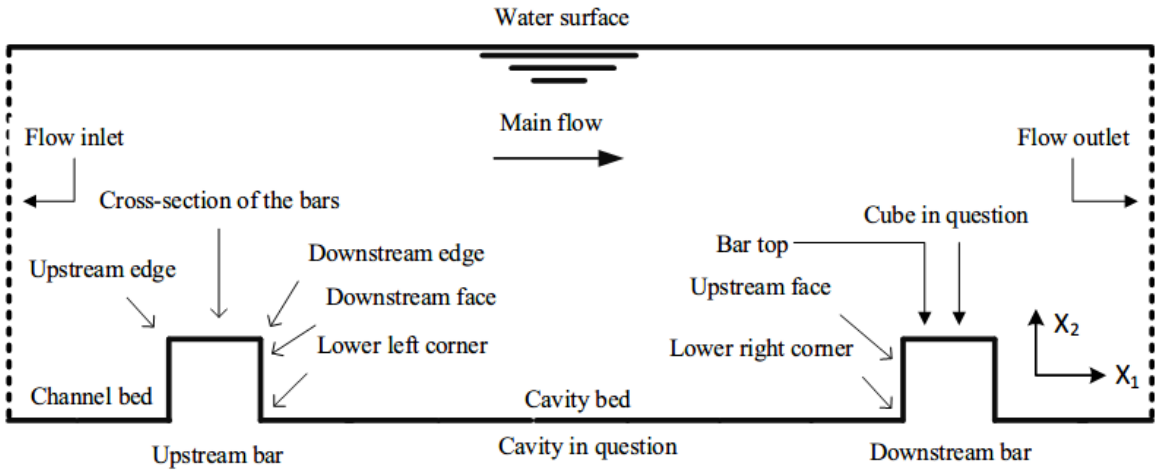

Figure 3-16 Side view of the vertical plane at the centreline of the channel (Figure 3-15). For clarity, only part of the model channel and two roughness elements are shown.

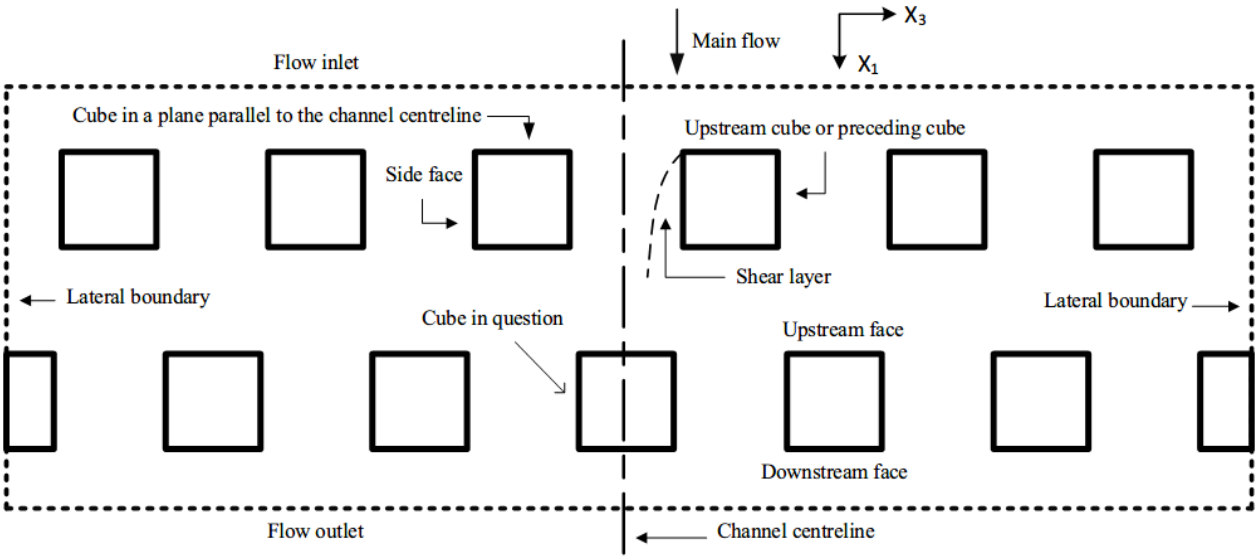

Figure 3-17 Top view of the model channels with rough elements (cubes) at the bed. The channel

centreline is located at x_3=0.0375.

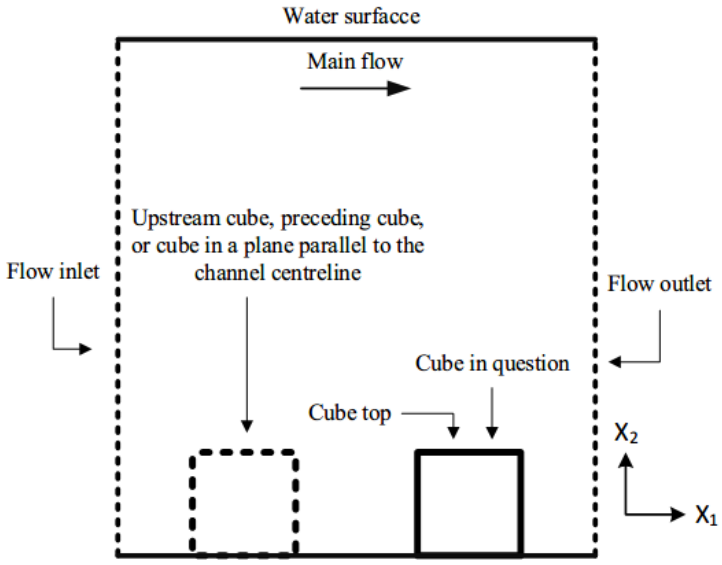

Figure 3-18 Side view of the vertical plane at the centreline of the channel (Figure 3-17).

No-slip boundary condition is applied at the channel-bed. The fluid sticks to the stationary boundary, has zero velocity, and does not seep through the bed. The condition is expressed as:

$$u_i = 0 \quad \text{(on channel beds)} \qquad [3\text{-}28]$$

This means that the resolved velocities in all three directions are zero at the channel bed.

The water surface is assumed to be a rigid lid. In reality, the water surface is free to deform under the influence of eddy motions. However, the computing costs will be prohibitively high if the water surface motions are to be captured. In this thesis, the water surface is fixed at x_2 = 0.075 m and does not deform.

A free-slip boundary condition is applied at the water surface. The shear stress at the water surface in the x_1- and x_3- directions are zero:

$$\tau_{12} = 0, \tau_{32} = 0 \quad \text{(on free surfaces)} \qquad [3\text{-}29]$$

This condition also means zero normal gradients of velocities at the water surface.

In order to minimise computing costs, cyclic conditions are applied between the channel inlet and

outlet, as well as between the two lateral boundaries in the transverse direction. Two pairs of periodic-shadow zones are created for circulating flow in both the streamwise and transverse directions. The velocity components at the outlet translate horizontally back to the inlet. The velocity components on one of the lateral boundaries translate horizontally back to the other lateral boundary:

$$u_i(\text{at the outlet}) = u_i(\text{at the inlet}) \qquad [3\text{-}30]$$

$$u_i(\text{at the left lateral boundary}) = u_i(\text{at the right lateral boundary}) \qquad [3\text{-}31]$$

The mass flow rates are specified for the applications of the periodic boundary conditions. The mass flow rates are 1.8138, 1.7138, 1.7138, and 1.517 kg/s for runs 1, 2, 3, and 4 (Tables 3-1 and 3-2), respectively. The corresponding freestream velocities are 0.367, 0.36, 0.407, and 0.407 m/s. The specified mass flow rates match the experimental conditions of Tachie & Adane (2007), which justifies direct a data comparison between the computer simulations from this thesis and their laboratory experiments.

3.5 Calculation of the Wall Distance

In this thesis, proper mesh was generated to cover the model channel, with local refinement for the near-wall areas. In these areas, the mesh must be fine enough to resolve the viscous sublayer. A key parameter is the distance from the centre of the first cell immediately off a wall (e.g. the channel-bed, bar surfaces, and cube surfaces) to the wall itself. For example, the wall distance of the first cell from the channel-bed should achieve the goal of $x_2^+ = 1$. The same goal applies to the first cell off the top surface of a transverse bar. Similarly, $x_1^+ = 1$ for the side surfaces of the bar. The method for calculating the wall distance of the first cell is discussed below:

The Reynolds number based on the characteristic scales of the flow is given by

$$\text{Re} = \frac{\rho U_e L}{\mu} \qquad [3\text{-}32]$$

where μ is the dynamic viscosity of water; U_e is the freestream velocity; L is the characteristic

length.

For the first cell off a solid wall in the x_1-direction (e.g. the side surfaces of a transverse square bar), the wall distance is

$$x_1^+ = \frac{\rho \, U_\tau \, \Delta x_1}{\mu} \qquad [3\text{-}33]$$

For the first cell off a solid wall in the x_2-direction (e.g. the top surface of a transverse square bar), the wall distance is

$$x_2^+ = \frac{\rho \, U_\tau \, \Delta x_2}{\mu} \qquad [3\text{-}34]$$

where U_τ is the frictional velocity; Δx_1 and Δx_2 are the normal distances of the first cell centres from the solid boundaries extending in x_2- and x_1-directions, respectively. The target values for x_1^+ and x_2^+, and the fluid property, are known apriori. So, one needs to calculate the frictional velocity U_τ, defined as

$$U_\tau = \sqrt{\frac{\tau_w}{\rho}} \qquad [3\text{-}35]$$

The wall shear stress, τ_w, can be calculated from the skin friction coefficient, C_f, as

$$\tau_w = \frac{1}{2} C_f \, \rho \, U_e^{\,2} \qquad [3\text{-}36]$$

The ambiguity in calculating Δx_1 surrounds the value for C_f. Empirical results have been used to provide an estimate of this value:

Internal Flows:

$$C_f = 0.079 \, \mathrm{Re}^{-0.25} \qquad [3\text{-}37]$$

External Flows:

$$C_f = 0.058 \, \mathrm{Re}^{-0.2} \qquad [3\text{-}38]$$

In this thesis, the C_f equation for external flow is used.

It is important to note that in cell-centre-based finite volume methods (Ansys Fluent, OpenFOAM), dependent values are stored in the centre of a finite volume. The size of the first cell is two times Δx_1 or Δx_2. In vertex-based (element-based) finite volume methods (Ansys CFX), dependent values are stored at the element nodes. The size of the first cell is equal to Δx_1 or Δx_2.

The characteristic length can be either the length of obstacles or the flow depth. Example calculations of the first cell size are listed in Table 3-3), using the flow depth as the characteristic length, and the obstacle length as the characteristic length. Because using the obstacle size as the characteristic length produces a smaller size, the first-cell size of 0.057 mm is used in this thesis.

Table 3-3 First cell heights for a variety of characteristic lengths

Target x_2+	Free stream velocity (m/s)	Characteristic length (m)	Viscosity (Ps·s)	First-cell size (mm)
1	0.4	0.075	8.9×10^{-4}	0.074
1	0.4	0.006	8.9×10^{-4}	0.057

3.6 **Grid Configuration**

Proper mesh are generated to cover model channels (Figures 3-19 to 3-27) and are locally refined for corners and near-wall areas. The mesh resolutions are selected based on the mesh independency tests and the recommendations from Choi and Moin (2012) and Gerasimov (2014). In the corners and near-wall areas, the flow is expected to change rapidly. The resolutions for other areas are relatively coarse. Rough surface flow is time-dependent. Thus, it is necessary to perform time discretisation of the filtered Navier-Stokes equations.

In Figure 3-19 to 3.23, the side view and front view of the mesh for Runs 1 (Tables 3-1 and 3-2) to 4, and Run 6 are shown. The Cartesian structure grids tidily cover the model channels. The grid sizes in the transverse direction for Run 1, 4, 5, and 6 is uniform, being 1.5 mm. The grid size in the transverse direction for Run 2 and 3 (Figure 3-26) is small (0.0008 m) in the centre but coarse (0.004 m) on the boundaries. For the region that is close to the channel-bed and rib surfaces, finer

grids resolve near-wall flow structures. The size of the first cell off the solid boundaries is such that $x_2^+ = 1$, or equal to 0.057 mm. The mesh sizes are coarser away from the edges of the bars and solid boundaries.

In Figures 3-23 and 3-25, the grid configuration for Run 5 (3D cubes) is shown, with an inflation layer of 3 mm at solid boundaries. The thickness of the inflation layer is similar to Run 4, shown in Figure 3-28. The first cell off solid boundaries satisfies $x_2^+ = 1$, the corresponding size being 0.057 mm. In the x_1- and x_3- directions, the sizes of the first cell range from 0.25 mm near the edges of bars to 0.5 mm in the middle of bars′ faces. Away from the solid surfaces, cells in the inflation layer increases in size at a prescribed growth rate. Outside the inflation layer, cells have a uniform size of 0.5 mm in the x_1- and x_2-directions, and varying sizes in the x_2-direction, at a growth rate of 1.1 until 2 mm at the water surface.

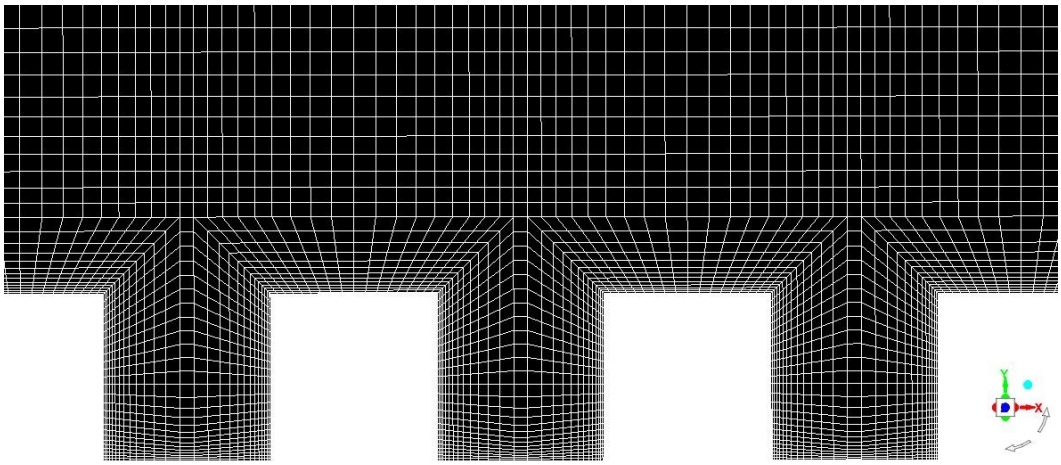

Figure 3-19 Side view of the mesh configuration for Run 1 (λ/k = 2). Summaries of all the runs

are in Tables 3-1 and 3-2.

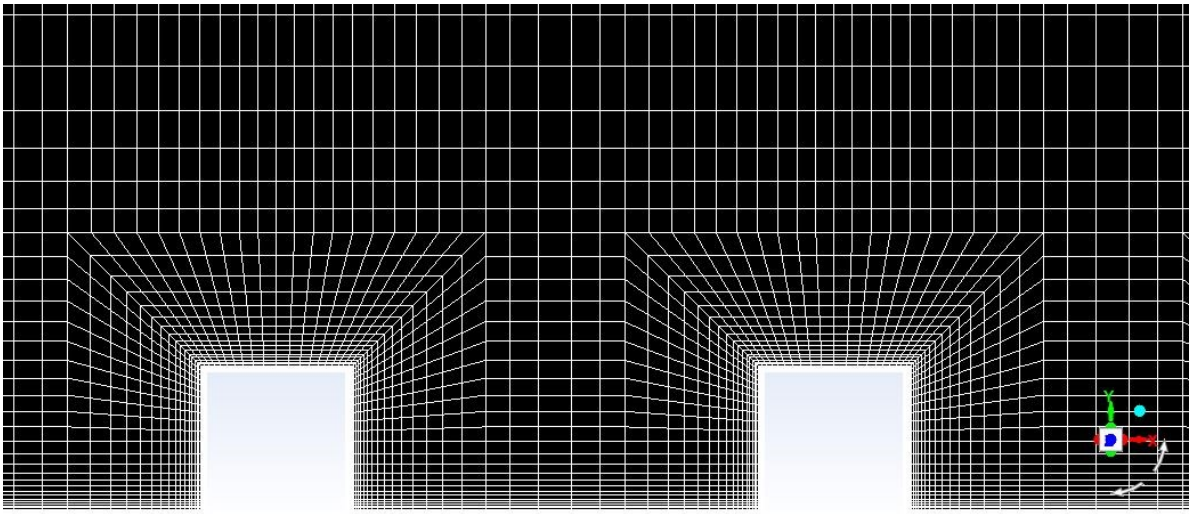

Figure 3-20 Side view of the mesh configuration for Run 2 (λ/k = 4).

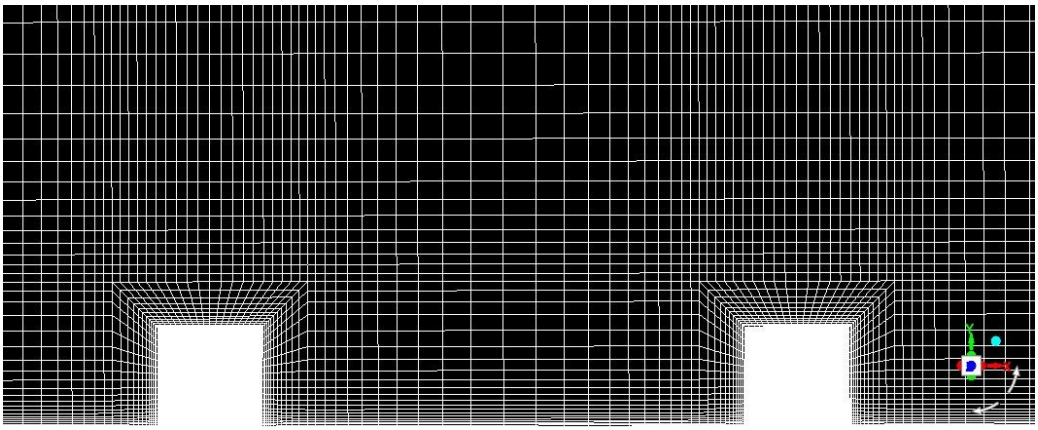

Figure 3-21 Side view of the mesh configuration for Run 3 (λ/k = 6).

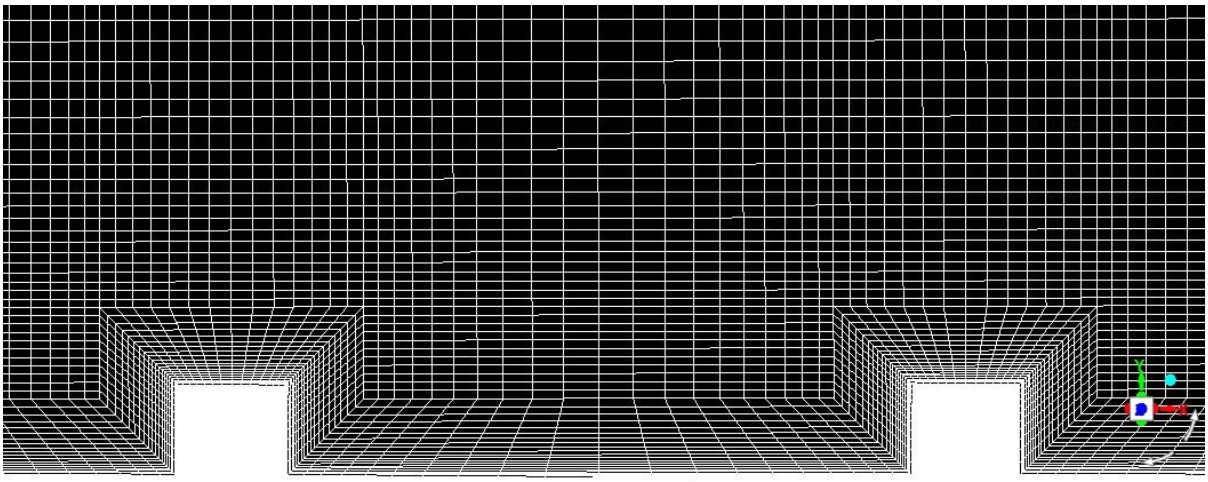

Figure 3-22 Side view of the mesh configuration for Run 4 (λ/k = 8).

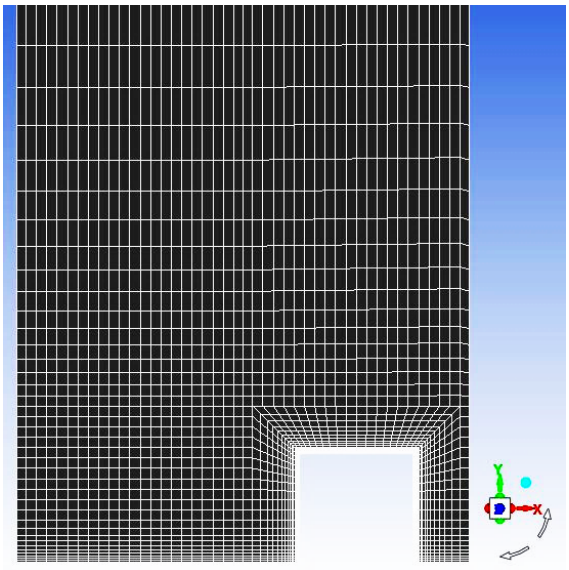

Figure 3-23 Side view of the mesh configuration for Run 5 (3-D cubes).

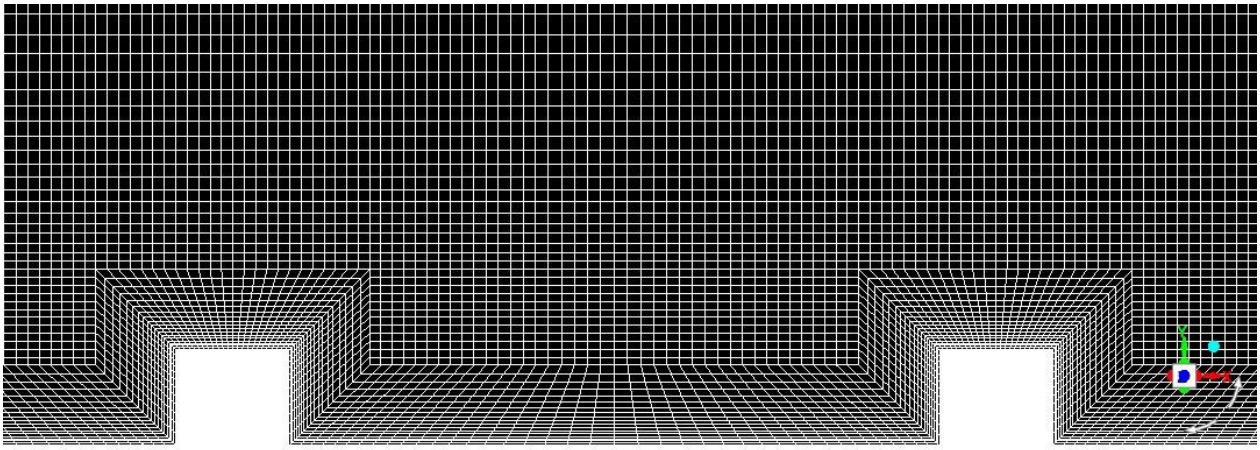

Figure 3-24 Side view of the mesh configuration used for Run 6 (λ/k = 8, for mesh independence test).

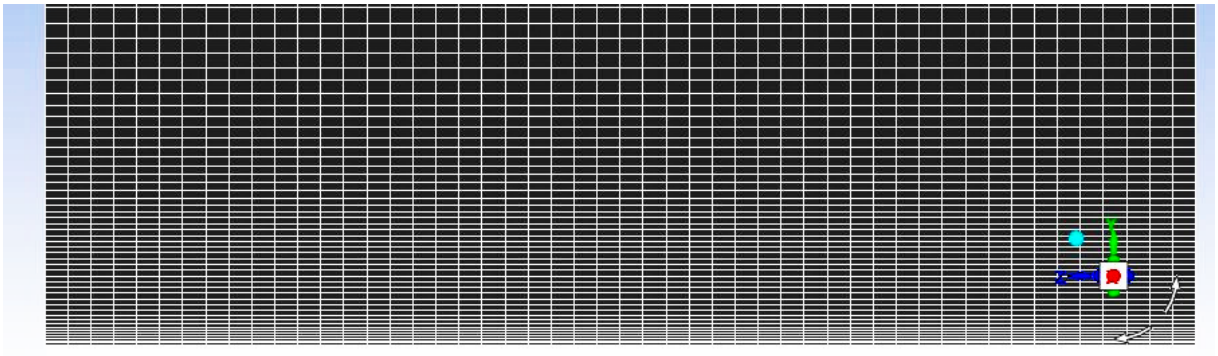

Figure 3-25 Front view of the mesh configuration for Run 1, 4, 5, and 6.

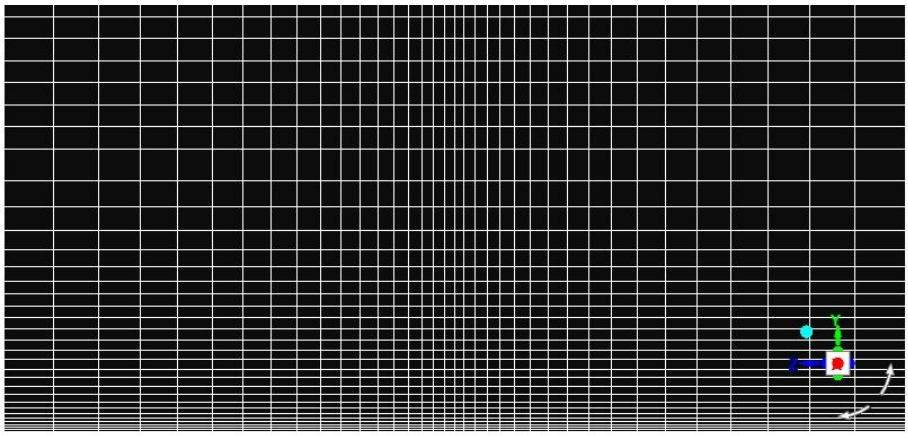

Figure 3-26 Front view of the mesh configuration for Run 2 and 3

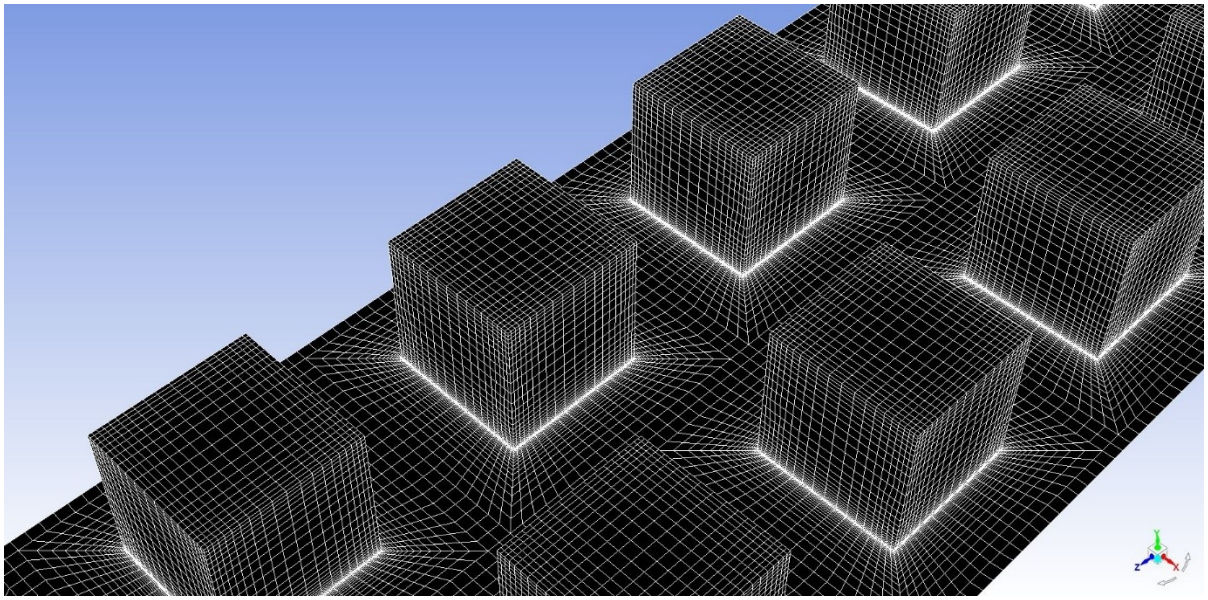

Figure 3-27 Mesh configuration of the channel-bed for Run 5 (3-D cubes).

As illustrated in Figure 3-28, four sub-regions are delineated to create the mesh for Run 4 (λ/k = 8). A similar process is followed to create the mesh for other runs. For the blue zone (Figure 3-28, bar tops), the height of the first cells off the solid boundaries meets the criterion of $x_2^+ = 1$, corresponding to 0.057 mm. The height of the cells increase at a growth rate of 1.2 in the direction normal to the walls, until they increase to 0.5 mm. The sizes of cells in the direction tangent to the walls vary from 0.25 mm around the bar's edges to 0.5 mm in the centres of the bar's faces.

For the red region (Figure 3-28, the cavity bed), the vertical size of the first cell off the solid boundaries is 0.057 mm, corresponding to $x_2^+ =1$. The height of the cells grow at a rate of 1.2 in the direction normal to the solid boundaries, to a maximum of 0.5 mm. The sizes of cells in the tangential direction range from 0.25 mm around the bar's edges to 1.5 mm in the centres of the cavities.

For the green region (Figure 3-28), individual cells have a constant vertical dimension of 0.5 mm. Their sizes in the tangential direction ranges from 0.25 mm on the boarder of the region to 1.5 mm in the centres of the cavities.

The grey region (Figure 3-28) is covered with cells of the same horizontal sizes as the blue and

green regions. Their vertical sizes increase from 0.5 to 3.5 mm at the water surface at a growth rate of 1.05.

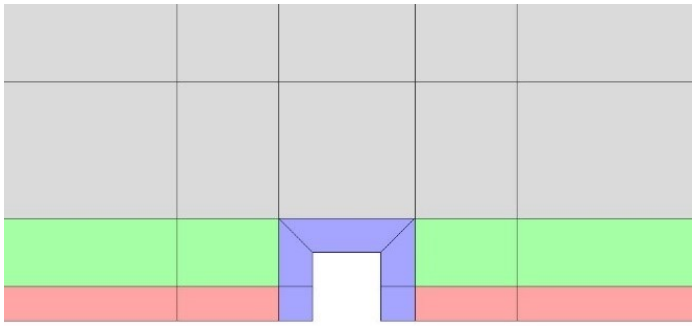

Figure 3-28 Four sub-regions delineated for creating cells of varying sizes.

Chapter 4
Results

The velocity profiles, and streamlines presented in this chapter are time averages of LES results over six seconds, after ten times the through-flow time. As an example, the time average of velocity components is taken as

$$U_j = \frac{1}{N}\sum_{i=1}^{N} u_j(x_1, x_2, x_3, t_i) \qquad [4\text{-}1]$$

where N is the total number of data points over the time period of 6 s. The data sampling frequencies for power spectrum and time series of velocity are different (Table 3-1). The free stream velocity, U_e, (Table 3-1) is used to normalise the velocities of the profiles.

The turbulence intensity, or the turbulence level presented in this chapter are estimated by a six seconds LES record. As an example, the estimation of turbulence intensity component is given by:

$$I_j = \frac{\sqrt{\frac{1}{N}\sum_{i=1}^{N} \Delta u_j(x_1, x_2, x_3, t_i)^2}}{U_e} \qquad [4\text{-}2]$$

$$\Delta u_j(x_1, x_2, x_3, t_i) = u_j(x_1, x_2, x_3, t_i) - \frac{1}{N}\sum_{i=1}^{N} u_j(x_1, x_2, x_3, t_i) \qquad [4\text{-}3]$$

where N is the number of records in the time series of velocity component at a given location; Δu_i is the time fluctuation of velocity in the x_i-direction; t_i is the time points at which records are taken; U_e is the time-averaged free stream velocity in the x_1-direction.

The Reynolds shear stress is defined as $-\overline{u_1 u_2}$. It can be calculated by:

$$-\overline{u_1 u_2} = -\frac{\sum_{1}^{N} u_1 u_2}{N} \qquad [4\text{-}4]$$

4.1 Independence of LES Results on Mesh

CFD model results should be independent of the mesh used. Usually, LES results are more accurate when using higher resolutions of mesh. Truly mesh-independent CFD results can only be achieved when the mesh is so fine that it actually resolves the flow field at the Kolmogorov scales. This section determines the resolution that is fine enough for LES of flow to capture the essential characteristics as observed from laboratory experiments, beyond which LES no longer produces significant changes to the flow characteristics.

Run 4 with 1689732 nodes (Figure 3-22, Tables 3-1 and 3-2) is compared to Run 6 with 2805000 nodes (Figure 3-24, Tables 3-1 and 3-2). For Run 4, the mesh resolution is based on the estimates of Choi and Moin (2012) and Gerasimov (2014), who suggested $\Delta x_1^+ \approx \Delta x_3^+ < 20$ to cover the region of interest (or above the top surface of bars). The cavity region has a maximum wall distance of $\Delta x_1^+ = 100$. For Run 6, the mesh resolution in x_1-direction (Figure 3-24) is two times denser than that for Run 4 ($\lambda/k = 8$, Figure 3-22). The mesh resolutions in x_2 and x_3 direction are the same between the two runs.

The comparison (Figure 4-1) shows slightly higher horizontal velocities for Run 6 than 4. It is unknown whether the time period of 6 s for average is long enough or not. In Figure 4-1, panel (a) is for the bar centre located at $x_1'/\lambda = 0$; panel (b) is for the centre-left of the cavity located at $x_1'/\lambda = 0.25$); panel (c) is for the middle of the cavity located at $x_1'/\lambda = 0.5$; panel (d) is the centre-right of the cavity located at ($x_1'/\lambda = 0.75$), where x_1' is given by

$$x_1' = x_1 - 0.264 \qquad [4\text{-}5]$$

meaning that x_1' equal to zero corresponds to the centre of the 6th bar (Figure 3-9).

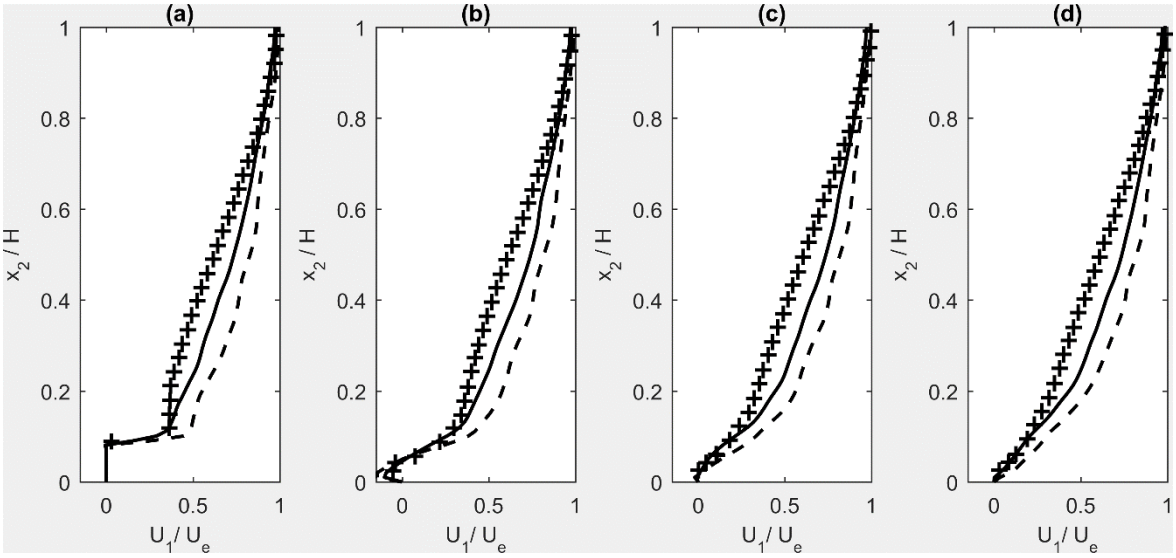

Figure 4-1 A comparison of vertical profiles of time-averaged horizontal velocity (U_1/U_e) between Runs 4 (solid curve) and 6 (dashed curve). Experimental data (Tachie & Adane, 2007) points are plotted as the plus symbols.

The comparison in Figure 4-2 shows slightly lower vertical velocities for Run 6 than 4. The velocity profile at the centre-left (panel a) of the cavity ($x_1'/\lambda = 0.25$) for Run 4 shows a velocity overshoot right above the channel-bed. Run 6 does not predict this feature of overshooting.

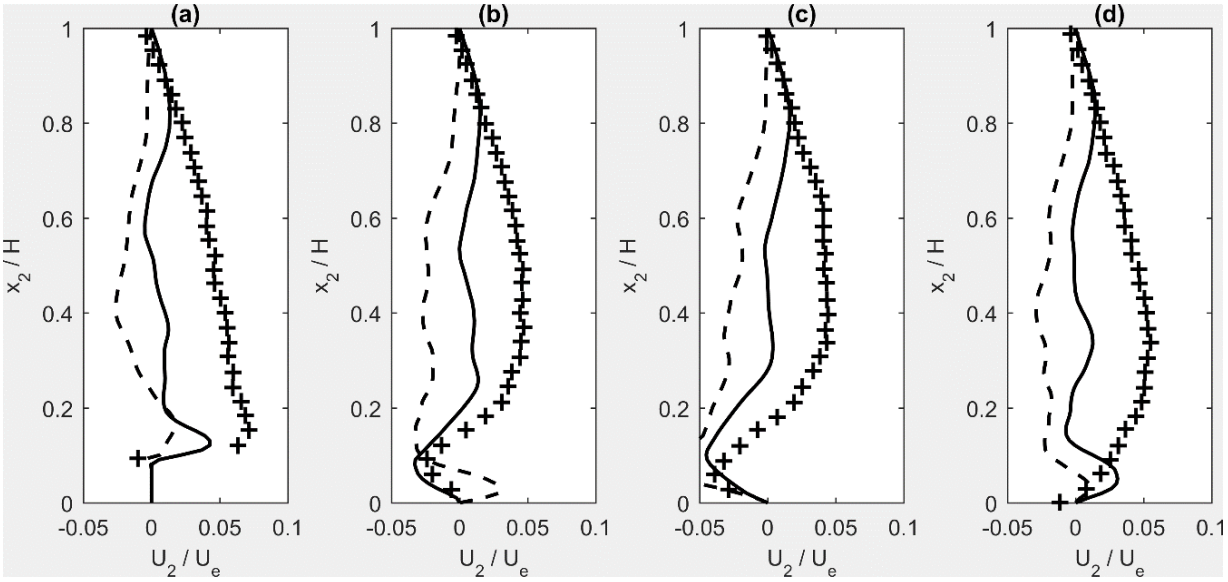

Figure 4-2 A comparison of vertical profiles of time-averaged vertical velocity (U_2/U_e). Symbols

and notations are the same as in Figure 4-1.

Figure 4-3 compares the vertical profiles of the time-averaged horizontal turbulence intensity (I_1/U_e) For Run 6, the turbulence intensity overshoots at the height of 0.1, while the overshoot for Run 4 occurs at the height of 0.3.

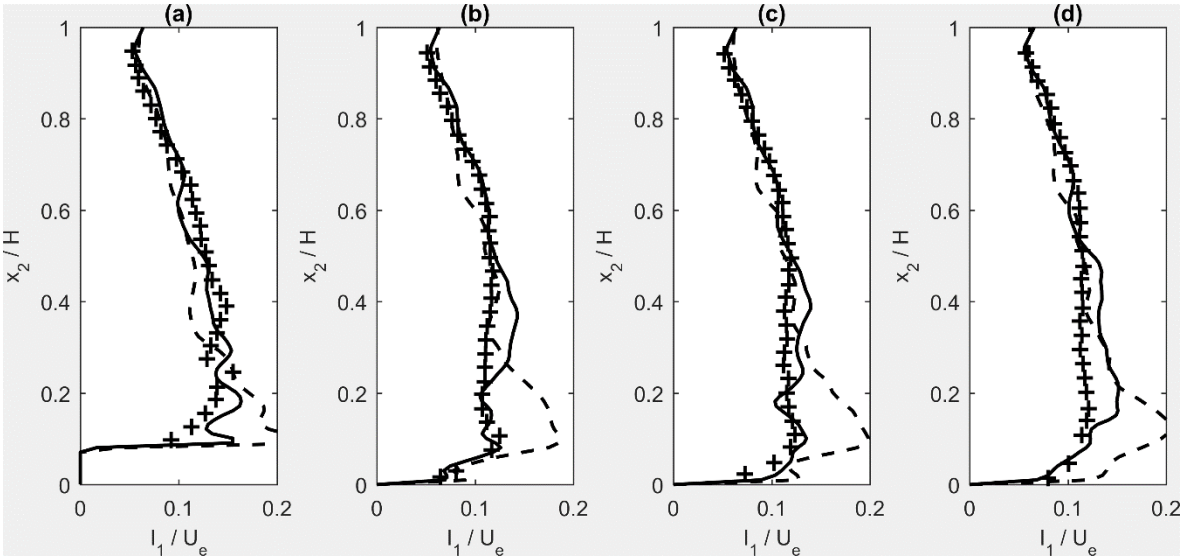

Figure 4-3 A comparison of vertical profiles of streamwise turbulence intensity (I_1/U_e). Symbols and notations are the same as in Figure 4-1.

Figure 4-4 compares the vertical profiles of the time-averaged vertical turbulence intensity (I_2/U_e). The curves for Runs 4 and 6 have similar shapes, except Run 6 gives a downward shift by a vertical distance of 0.05, compared to Run 4.

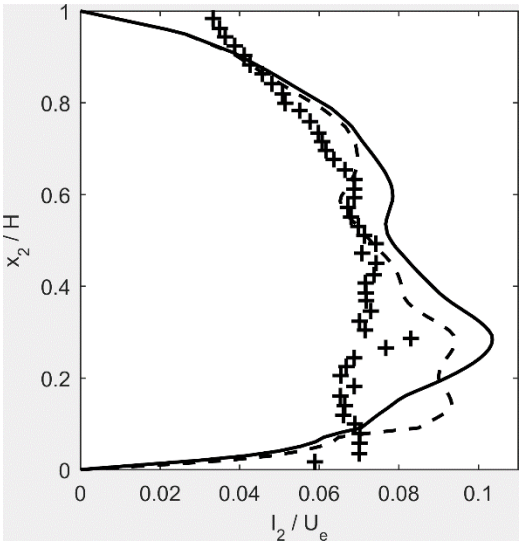

Figure 4-4 A comparison of vertical profiles of vertical turbulence intensity (I_2/U_e). Symbols and notations are as in Figure 4-1.

Figure 4-5 compares vertical profiles of the Reynolds shear stress ($-\overline{u_1 u_2}/U_e$). Similar to Figure 4-4, the Reynolds shear stress curves for Runs 4 and 6 have similar shapes. For Run 6, there is a downward shift by a vertical distance of 0.1, compared to that for Run 4.

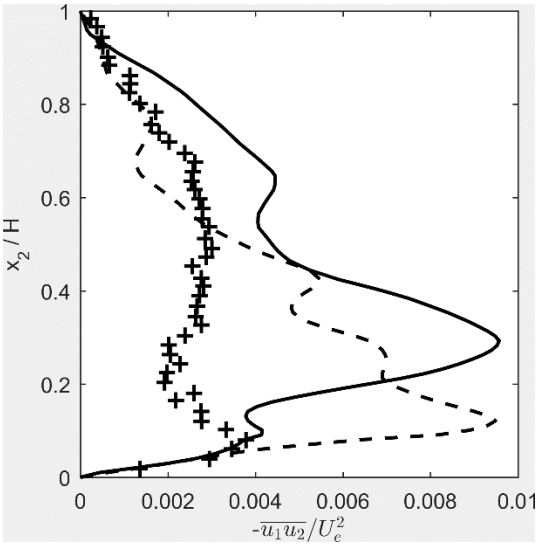

Figure 4-5 A comparison of vertical profiles of Reynolds shear stress ($-\overline{u_1 u_2}/U_e$). Symbols and notations are the same as in Figure 4-1.

Runs 4 and 6 show slight differences in time-averaged horizontal and vertical velocities, vertical

turbulence intensity, and Reynolds shear. For both runs, there are overshoots of streamwise turbulence intensity at a certain vertical position. Run 4 appears to match the experiments better than Run 6. There are no significant differences between the two runs. Therefore, the mesh of Run 4 is suitable for simulating k-type roughness flow.

4.2 Velocity Profiles

In turbulent flow, turbulent eddies create fluctuations in velocity. The instantaneous velocity can be decomposed into mean velocity and turbulent fluctuation. It is important to verify the LES model by a comparison of mean velocity profiles between simulations and experiments.

Figures 4-6 and 4-7 compare the mean streamwise velocity profiles between Run 1 (λ/k = 2, d-type roughness flow, Tables 3-1 and 3-2) and experiments. The velocity profiles are for: (a) the bar centre ($x_1'/\lambda = 0$), (b) the middle of the cavity ($x_1'/\lambda = 0.5$), (c) the centre-right of the cavity ($x_1'/\lambda = 0.75$). Here, x_1' is defined by $x_1' = x_1 - 0.078$ m ($x_1 = 0.078$ m is the centre of the 7th bar). The velocity profiles are representative because of the nearly identical flow characteristics at each corresponding bar section. For clarity, only the velocity profiles in the section of the 7th bar are shown.

The LES predictions match the experimental data very well, shown as the curves and the plus symbols (Figures 4-6 and 4-7) with the same shapes. The maximum differences of the curves and the plus symbols fall within 5%. There are discrepancies. In the boundary shear layer, the velocity is over-predicted, and hence the bed shear stress may have been under-predicted.

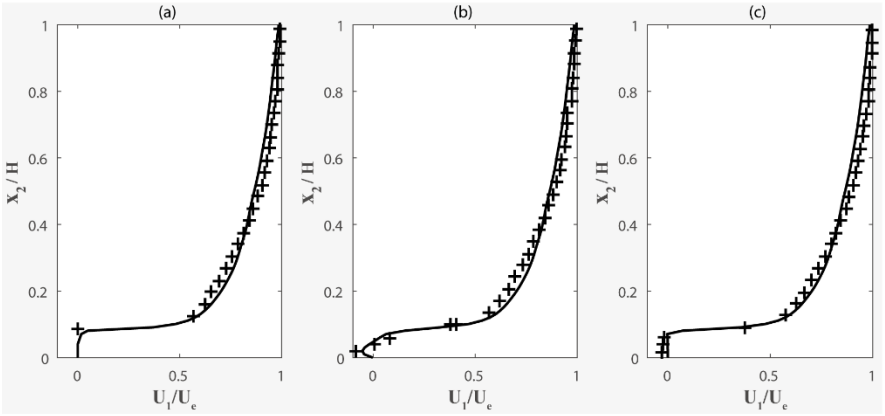

Figure 4-6 A comparison of mean streamwise velocity profiles (U_1/U_e) between Run 1 (solid curve) and the experiments (plus symbol).

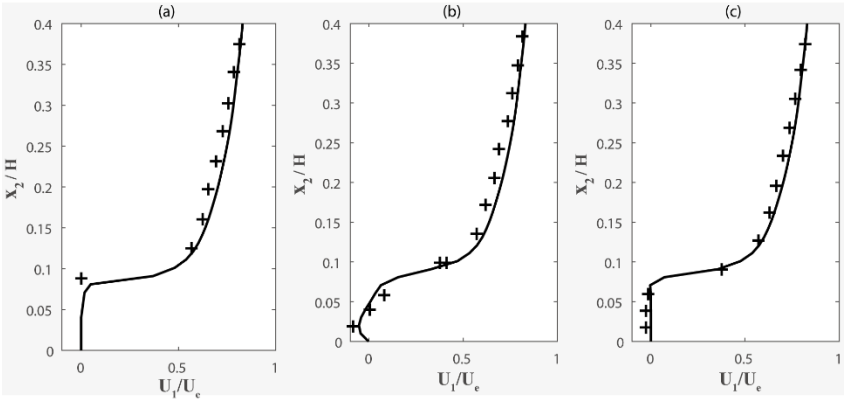

Figure 4-7 close-up view of Figure 4-6. Symbols and the locations of the profiles in the panels are the same as in Figure 4-6.

Figure 4-8 compares the mean vertical velocity profiles of Run 1 with the experimental data. The locations of the corresponding profiles in panels are the same as in Figure 4-6. The predicted vertical velocity profiles deviate from the experimental data. A probable reason is the restriction of the rigid lid approximation. On the other hand, the experimental data seem to have unexplained features near the water surface. The vertical velocity at the free surface is supposed to be zero, because fluid elements are not expected to be able to move across the water surface. At the macroscale, the incoming flow through the inlet should be equal to the outgoing flow through the outlet, and thus one expect $\frac{\partial U_2}{\partial x_2} = 0$. However, this is not the case for the experimental data.

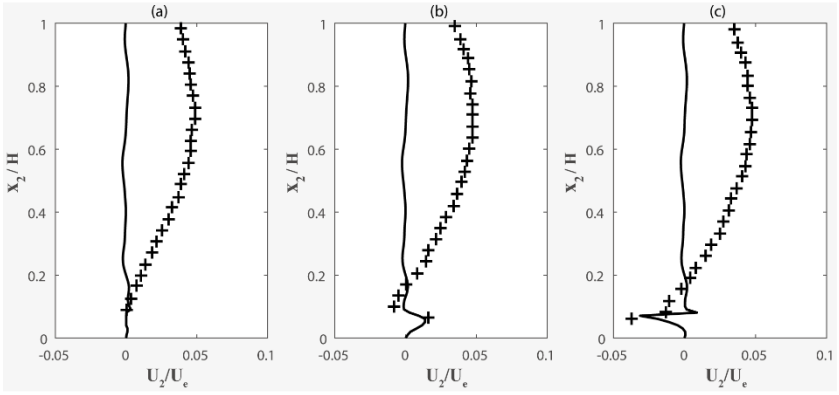

Figure 4-8 A comparison of mean vertical velocity profiles (U_2/U_e) between Run 1 and the experiments. Symbols and the locations of the profiles in the panels are the same as in Figure 4-6.

Figures 4-9 and 4-10 compare the mean streamwise velocity profiles of Run 4 (λ/k = 8, k-type roughness flow, Tables 3-1 and 3-2) with the experimental data. The velocity profiles are for: (a) the bar centre ($x_1'/\lambda = 0$); (b) the centre-left of the cavity ($x_1'/\lambda = 0.25$); (c) the middle of the cavity ($x_1'/\lambda = 0.5$); (d) the centre-right of the cavity ($x_1'/\lambda = 0.75$). Here, x_1' is defined as $x_1' = x_1 - 0.264$ ($x_1 = 0.264$ m is located at the centre of the 6th bar).

In Figures 4-9 and 4-10, the LES predictions of vertical profiles of the mean horizontal velocities (the curves) match the observed profiles (the plus symbols) very well. The maximum differences of the curves from the plus symbols fall within 15%. The predicted and observed profiles have the same shapes. However, there are some discrepancies, one being the transition point in the boundary shear layer (shown as "a" in Figure 4-9).

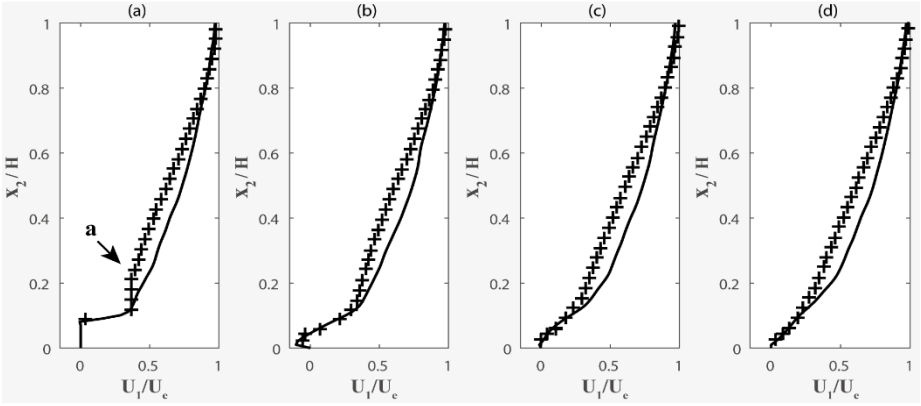

Figure 4-9 A comparison of the mean streamwise velocity profiles (U_1/U_e) between Run 4 (solid

curves) and the experiments (plus symbols).

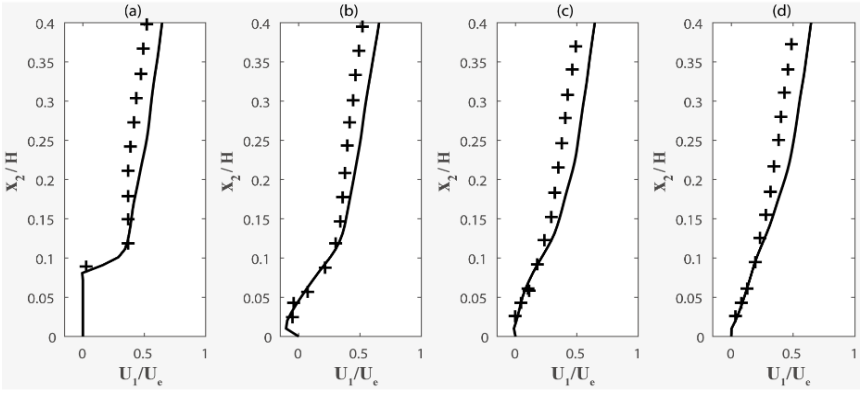

Figure 4-10 close-up view of Figure 4-9. Symbols and the locations of the profiles in the panels are the same as Figure 4-9.

Figure 4-11 compares the mean vertical velocity profiles of Run 4 with the experimental data. The locations of the profiles in the panels are the same as in Figure 4-9. The predicted vertical velocity profiles in the near-bed region ($0 < x_2/H < 0.3$) roughly match the experimental data. More precisely, the LES provides accurate predictions for the cavity, but less accurate for a small region just upstream of the bar (panel d) and above the bar (panel a). The predicted vertical velocity profiles in the main flow region ($0.3 < x_2/H < 0.8$) show different trends, compared to the experimental data. In this region, there are more significant upward motions in the experiments than the simulation. The predicted vertical velocity profiles in the near water surface region match well with the experimental data.

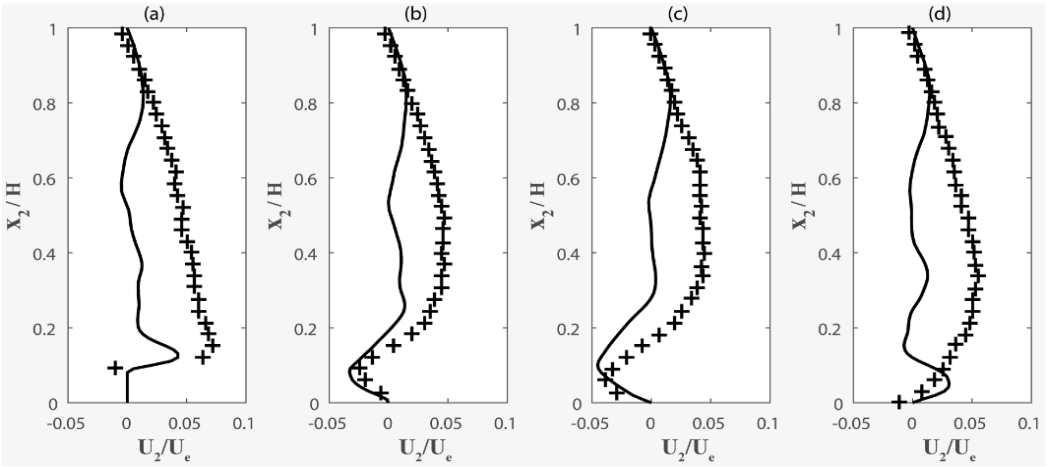

Figure 4-11 A comparison of the mean vertical velocity profiles (U_2/U_e) of Run 4 to the

experiments. Symbols and the locations of the profiles in the panels are the same as in Figure 4-9.

In summary, the LES predicts mean streamwise velocities accurately for both the d-type and k-type roughness flows, especially for the near-bed region. The LES roughly predicts the mean vertical velocity. The predictions roughly match the experimental data for the near-bed region, but show different trends from the experimental data for the main stream and water surface regions.

It seems that the large eddy simulations have produced accurate flow characteristics in the streamwise direction, but less accurate results in the vertical direction. A plausible reason is the sidewall effects. It is challenging to realistically capture secondary flow that creates transverse vortices in the transverse direction on both sides of the channel. These vortices cause upward motions in the middle of the channel.

4.3 Turbulence Intensity

Figure 4-12 compares the streamwise turbulence intensity, I_1, for Run 1(d-type roughness flow, $\lambda/k=2$, Table 3-1 and 3-2) with the experimental data. The locations of the corresponding profiles in the panels are the same as in Figure 4-6. I_1 is given in Equations [4-2] and [4-3]. The velocity profiles are representative because of the nearly identical flow characteristics at each corresponding bar section. For clarity, only the turbulence intensity in the section of the 7^{th} bar is shown. In panel (b), the turbulence intensity is relatively small in the cavity with a peak value of 0.035 right above the channel-bed. In all the three panels, the turbulence intensity grows quickly to a maximum of 0.12 over a short distance right above the roughness height. It then drops abruptly to 0.06 at $x_2/H = 0.2$. Further up, it gradually drops to 0.05 at the free water surface. The LES predictions match the experimental data very well. The predictions show more fluctuations in the lower half of the water column. I_1 values become larger to form the peak in the shear layer region, and become smaller at a higher elevation above the bar top.

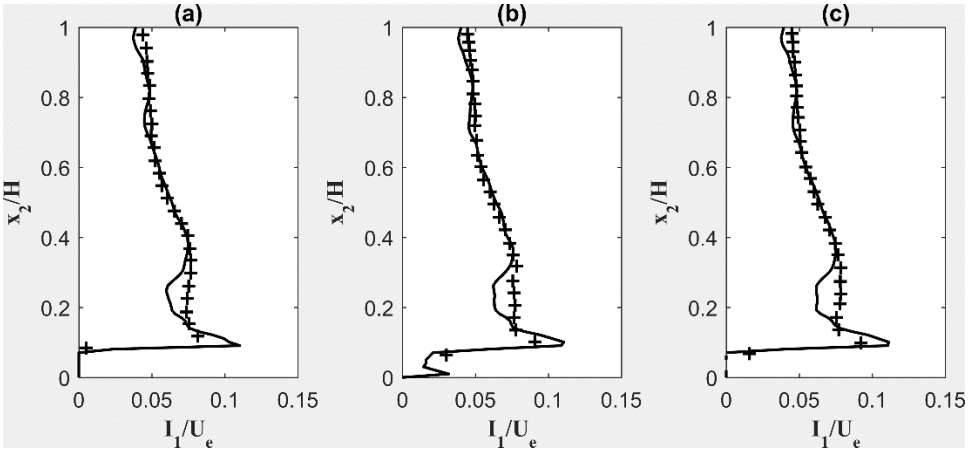

Figure 4-12 A comparison of the streamwise turbulence intensity between Run 1 and the experiments. Symbols and the locations of the profiles in the panels are the same as in Figure 4-6.

Figure 4-13 compares the streamwise turbulence intensity for Run 4 (k-type roughness flow, λ/k=8, Table 3-1 and 3-2) with the experimental data. The locations of the corresponding profiles in the panels are the same as in Figure 4-9. In the experimental data, the streamwise turbulent intensities for the cavity section (panels b, c, d) are different from those for the bar section (panel a). For the cavity section, the turbulence intensity is about 0.09 on the channel-bed. Then it grows to a maximum of 0.11 at the roughness height. The turbulence intensity stays at the maximum value over a large vertical distance until $x_2/H = 0.6$. Then it gradually drops to 0.05 at the water free surface. On the bar top, the turbulence intensity dramatically increases from zero to a maximum of 0.16 over a short vertical distance. Then it fluctuates around the maximum value until $x_2/H = 0.5$. The turbulence intensity then gradually drops to 0.05 at the water surface. The predicted streamwise turbulence intensity roughly matches the experimental data. Clearly, the LES provides accurate results in cavities and near water surface. In the cavity section, the turbulence intensity is over-predicted by 0.02 at $x_2/H = 0.4$. In the bar section, the turbulence intensity is predicted accurately at $x_2/H = 0.4$. The experimental data of I1 and LES results show the same amplitude of fluctuations.

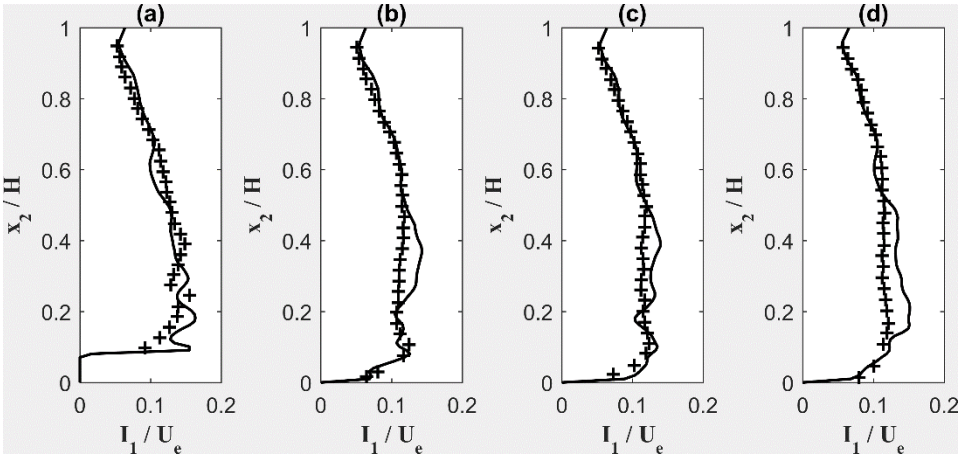

Figure 4-13 A comparison of the streamwise turbulence intensities of Run 4 with experiments. Symbols and the locations of the profiles in the panels are the same as in Figure 4-9.

Figure 4-14 compares the vertical turbulence intensity, I_2, for Run 1 with the experimental data. I_2 is spatially averaged over a pitch, starting from $x_1 = 0.078$ m, which is the centre of the 7th bar. In the experimental data, I_2 under the roughness height is relatively small. It increases rapidly in the region right above the roughness height. After reaching a maximum of 0.05, I_2 drops gradually. Then it levels off at a value of 0.04 from $x_2/H = 0.5$ to the water surface. The LES predictions of I_2 are very approximate for the lower half of the water column. The LES matches the experiments in terms of the maximum value of I_2 above the roughness height. However, the LES profiles show an extra peak of 0.05 at the height of $x_2/H = 0.6$, which is not seen from the experimental data. The experimental data seem to be inaccurate at the water surface, because the turbulence intensity there is supposed to be around zero.

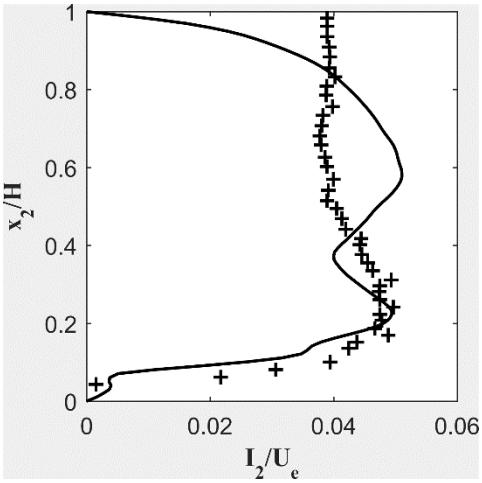

Figure 4-14 A comparison of the vertical turbulence intensity between Run 1 (solid curve) and the experiment (plus symbol).

Figure 4-15 compares the vertical turbulence intensity, I_2, for Run 4 with the experimental data. I_2 is spatially averaged over a pitch, starting from $x_1 = 0.264$ m, which is the centre of the 6th bar. In the experimental data, the vertical turbulence intensity increases steadily under the roughness height. A peak value of 0.08 happens right above the roughness height. Then it drops slightly, and recovers to form a maximum of 0.09. After this point, I_2 drops gradually to 0.03. Compared with the experiments, the LES provides relatively accurate predictions. I_2 near the free surface is under-predicted. Except for this region, I_2 in the main stream area and near the channel-bottom is generally over-predicted by 0.01.

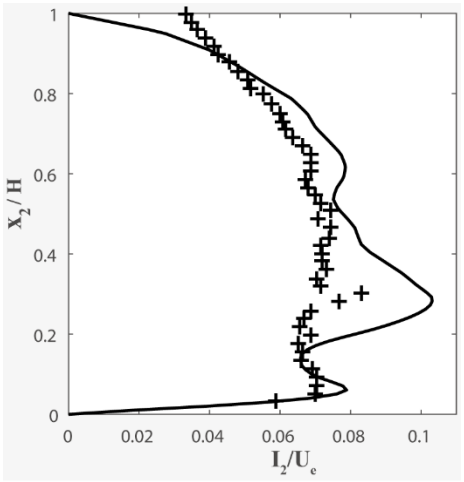

Figure 4-15 A comparison of the vertical turbulence intensities between Run 4 (solid curve) and the experiment (plus symbol).

4.4 Reynolds Shear Stress

In Figure 4-16, the normalised Reynolds shear stress for Run 1 (d-type roughness flow, λ/k=2, Table 3-1 and 3-2) is compared to the experimental data. The quantity is spatially averaged over a pitch, starting from $x_1 = 0.078$ m, which is the centre of the 6th bar. The measured normalised Reynolds shear stress is relatively low below the roughness height. Over the roughness height, the measured normalised Reynold shear stress increases dramatically over a very short distance, to a

value of 0.001. Then it increases to a maximum of 0.0019 at $x_2/H = 0.3$, with some fluctuations. After this point, the quantity slowly drops to 0.1, and levels off from $x_2/H = 0.6$ to the free water surface. LES accurately predicts the Reynolds shear stress for the lower half of the water column, but over-predicts it for the upper half. Above the roughness height, the predictions show spatial fluctuations, which have essentially the same amplitude as those seen from the experimental data over the lower half of the water column. The local peak values as well as their elevations of occurrences are the same between LES and the experiments. For the upper half of the water column, the predictions show slightly fluctuating Reynolds shear stresses over a large vertical distance. Further upward, LES over-predicts the Reynolds shear stress. Then the predicted Reynolds shear stress drops to zero near the water surface. Near the free water surface, the Reynolds shear stress is under-predicted because of the rigid-lid approximation.

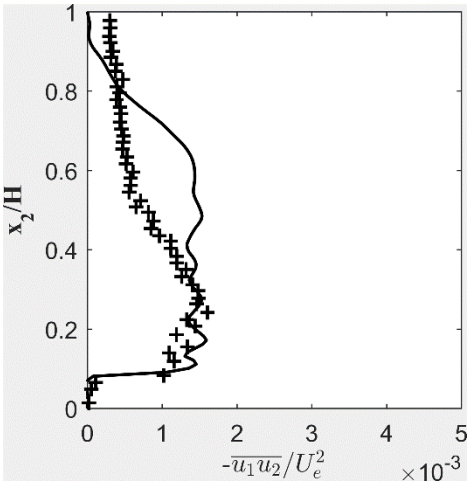

Figure 4-16 A comparison of the Reynolds Shear Stress of Run 1 to the experiments. Symbols and the location of the profile in the panel are the same as in Figure 4-14.

Figure 4-17 compares the Reynolds shear stress for Run 4(k-type roughness flow, λ/k=8, Table 3-1 and 3-2) to the experimental data. The Reynolds shear stress is averaged over a pitch, starting from $x_1 = 0.264$ m (the centre of the 7th bar). In the experiments, the Reynolds shear stress increases to a maximum of 0.004 at the roughness height from zero at the channel-bed; it drops to 0.002 at $x_2/H = 0.2$. Further up, it changes with a parabolical trend, reaching 0.003 at $x_2/H = 0.5$, and back to zero near the water surface. Compared with the experimental data, the LES predictions are accurate for the region below the roughness height, but are too high for the region above. The predictions and measurements are the same at the roughness height. Above the roughness height,

the predicted Reynolds shear stresses increase dramatically to 0.01, nearly 2.5 times the measured maximum value. The predicted Reynolds shear stresses drop to zero at the water surface.

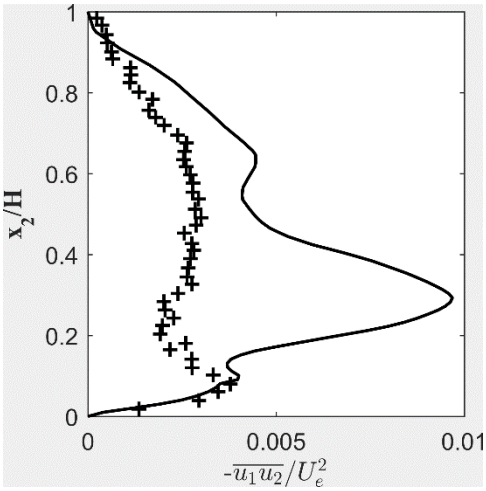

Figure 4-17 A comparison of the Reynolds Shear Stress of Run 4 to the experiments. Symbols and the location of the profile in the panel are the same as in Figure 4-15.

4.5 Time Series of Streamwise Velocity

Time series of the horizontal velocity component, U_1, for Run 1 (d-type roughness flow, λ/k=2, Table 3-1 and 3-2) are plotted in Figure 4-18 (a)-(w) for 23 selected locations, 21 of which are marked in Figure 4-19. The (x_1, x_2) coordinates of the other two locations are: (0.081 m, 0.037 m) and (0.081 m, 0.075 m). These U_1 time series exhibit no overall trend of increase or decrease. In other words, the velocity components are at a state of equilibrium over a time period of 6 s. It is understood that the individual equilibrium values are different from location to location.

In Figure 4-18 (a)-(e), at the elevation of x_2 = 0.001 m (or 1 mm above the cavity bed), each of the five time series shows three troughs with a magnitude significantly lower than the mean value of U_1. U_1 is larger than the mean value for a certain time span between adjacent troughs.

In contrast to the patterns seen from Figure 4-18 (a)-(e) for locations at 1 mm above the bar bar top, the six time series of U_1 at 6 mm above the cavity bed each show three spikes [Figure 4-18 (q)-(u)]. Between these spikes, the U_1 has values lower than the mean. The troughs and spikes

occur at the same frequency, being 0.5 Hz. However, the spikes are more profound, associated with higher mean velocities and higher turbulence intensity.

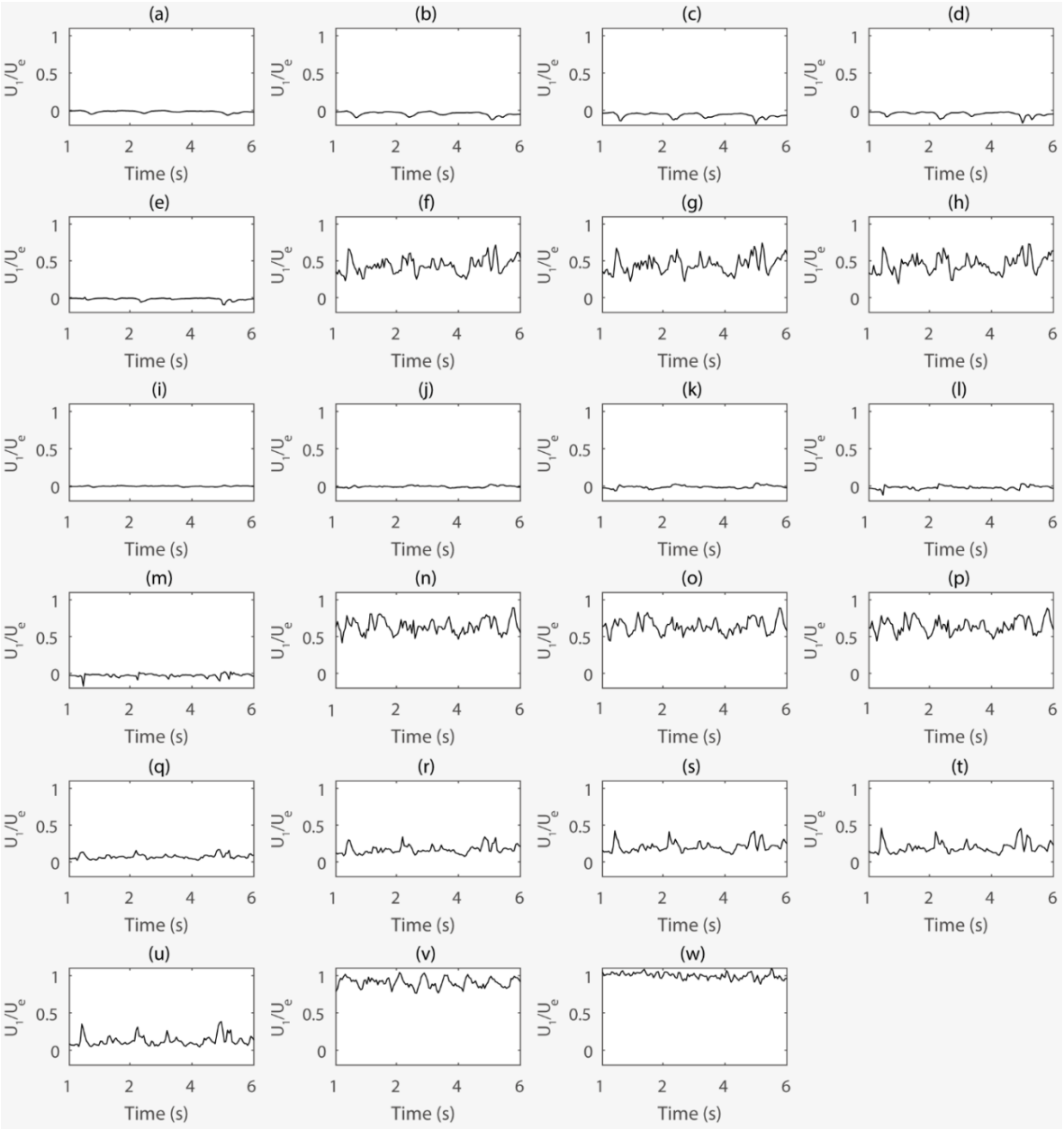

Figure 4-18 Time series of horizontal velocity for Run 1 at 23 selected locations.

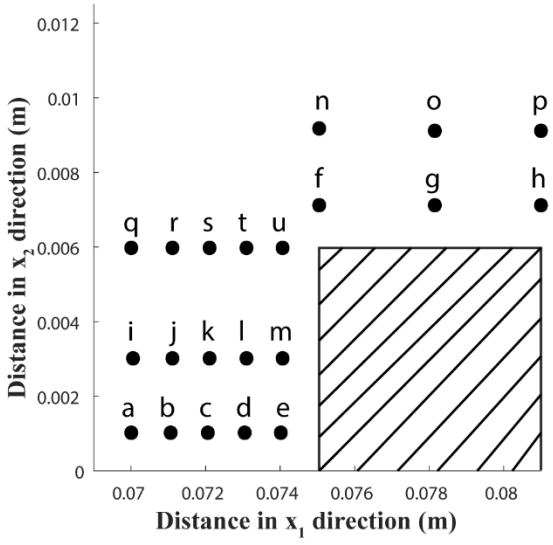

Figure 4-19 Locations for which time series of U_1 are plotted in Figure 4-18.

4.6 Flow Patterns in Vertical Plane

The streamlines of flow in the vertical plane at the channel centreline for Run 1 (λ/k = 2, Tables 3-1 and 3-2) are shown in Figure 4-20. The streamlines of all the runs are representative because of the nearly identical flow characteristics at each corresponding bar section. For clarity, only the portion from x_1 = 0.069 to 0.081 m, including the 7th bar, is shown in Figure 4-20. The predicted streamlines show a variety of eddy structures in the cavities and above the bar tops. The fluid circulation of the main flow above the bar is virtually isolated from the flow in the cavity. A small eddy forms in each of the two lower corners of the cavity (Figures 3-15 and 3-16), but the associated fluid circulation is insignificant, in comparison to that associated with the dominant eddy. The two small eddies have more or less the same strength. In the dominant eddy, fluid circulation is counter-cyclonic, whereas in the small eddy, the fluid circulation is cyclonic. The streamlines over the cavity is horizontal.

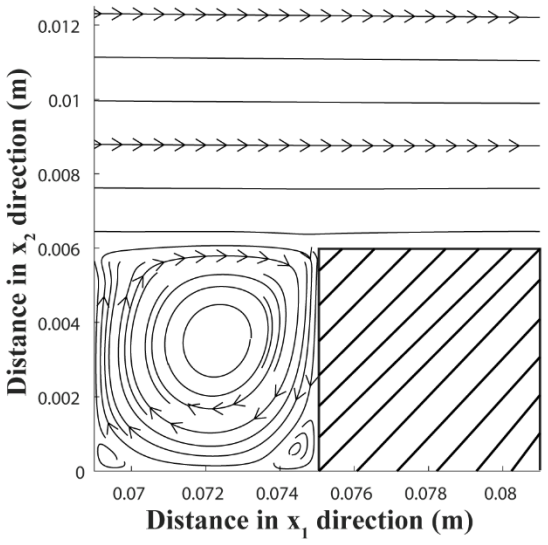

Figure 4-20 Streamlines at the channel centreline (the vertical plane of $x_3 = 0.0375$ m) for Run 1.

Contours of the horizontal velocity component, U_1, for Run 1 is shown in Figure 4-21 for the same plane as Figure 4-20. U_1 of all the runs are normalized by the free stream velocity U_e (equal to 0.4 m/s). U_1 is relatively small in the cavity, compared with that above the bar height. The narrowness of the cavity blocks the fluid inside the cavity from circulating into the main flow. Above the cavity, U_1 increases in strength quickly over a short vertical distance. The shear layer is flat and thin.

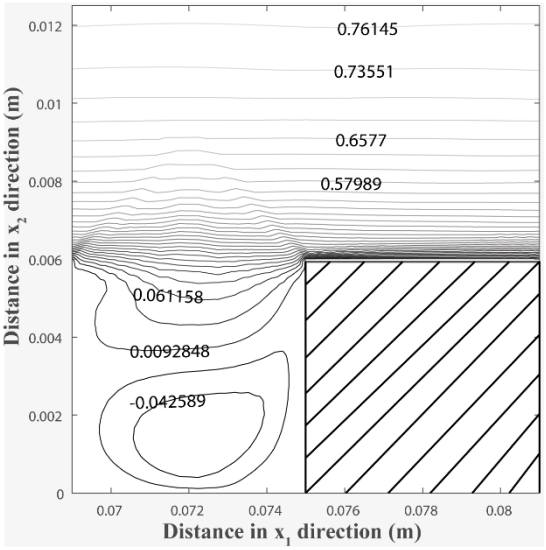

Figure 4-21 Contours of the horizontal velocity component U_1 for Run 1.

The streamlines of flow for Run 2 (λ/k = 4) shown in Figure 4-22 are similar to those for Run 1.

For clarity, only the portion from x_1 = 0. 0625 to 0. 0875 m, including the 4th bar, is shown. Three eddies appear in the cavity. Two of them form in each of the two lower corners of the cavity, and a dominant eddy forms in the middle. Compared to that for Run 1, the eddy in the lower left corner is significantly larger and stronger than that in the lower right corner. Due to the presence of the relatively large eddy in the lower left corner of the cavity, the dominant eddy is distorted on the upstream side, circulating fluid over only the upper one half of the bar height. The dominant eddy maintains a regular shape on the downstream side.

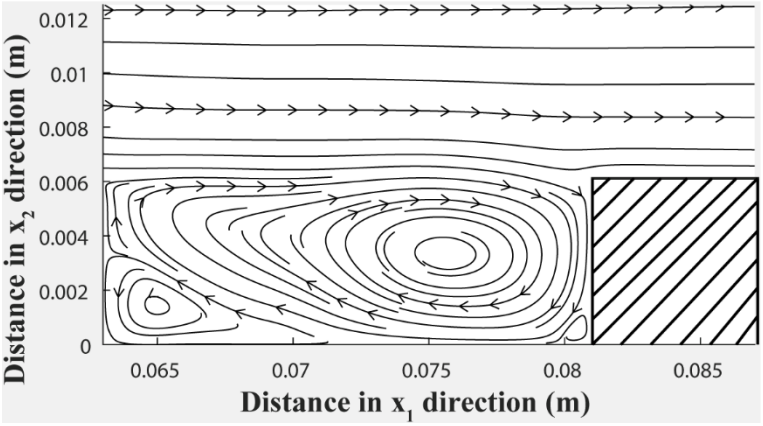

Figure 4-22 Streamlines of flow at the centreline of the channel for Run 2.

Contours of the horizontal velocity component, U_1, for Run 2 (λ/k = 4) are shown in Figure 4-23 for the same vertical plane as Figure 4-22. The contours converge at the upstream edge of the bar (Figures 3-15 and 3-16), remain parallel to the top surface, start to diverge from the downstream edge of the bar, and converge toward the upstream edge of the next bar. The dominant eddy gives rise to almost as strong reverse flow as the velocities above the bar top. Due to the influence of the cavity, the shear layer is thicker and somewhat wavy, compared with that for Run 1.

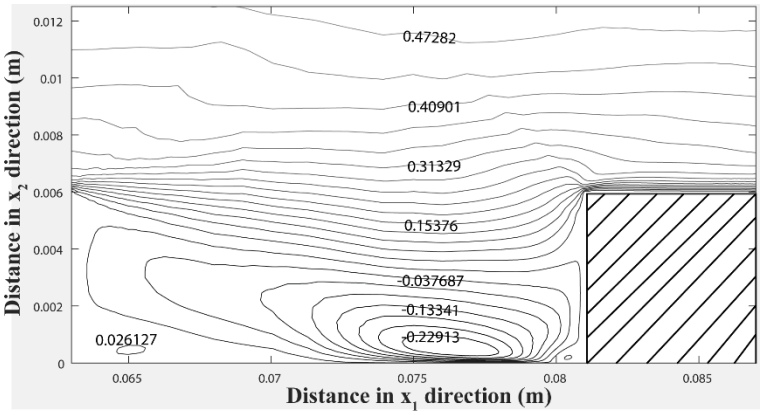

Figure 4-23 Contours of the horizontal velocity component U_1 for Run 2.

The streamlines of flow for Run 3 (λ/k = 6) are shown in Figure 4-24 for the centreline vertical plane between x_1 = 0. 0575 and 0. 0925 m, including the 3rd bar. The streamlines show no dense distributions near the cavity-bed. To some extent, flow separations occur in the lower corners of the cavity. The streamlines of the mainstream flow have no contact with the cavity-bed. Differences and similarities between Runs 3 and 2 are commented below. Compared to the dominant eddy (Figure 4-22) for Run 2, the dominant eddy (Figure 4-24) shifts its centre towards the upstream bar. Between Figures 4-22 and 4-24, the secondary eddy in the lower corner is larger and stronger for Run 3 than Run 2. Run 3 produces a new eddy (Figure 4-24) in the lower right corner, which is not present in Figure 4-22 for Run 2. For Run 3, the two secondary eddies in the lower corners interact with the dominant eddy in the cavity and with the mainstream flow.

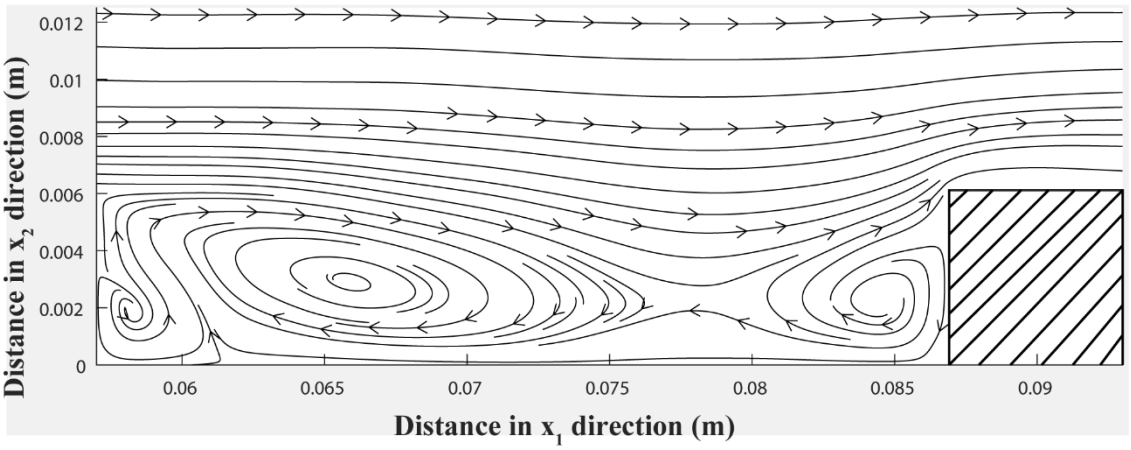

Figure 4-24 Streamlines of flow at the channel centreline for Run 3.

Contours of the horizontal velocity component, U_1, for Run 3 is shown in Figure 4-25 for the same plane as Figure 4-24. The contours show converging and diverging patterns similar to those (Figure 4-23) for Run 2. However, the reverse flows associated with the eddies in the lower half of the cavity merge to generate a long, narrow strip near the channel floor. The reverse flows are much weaker than those for Run 2. The shear layer for Run 3 is thick and wavy.

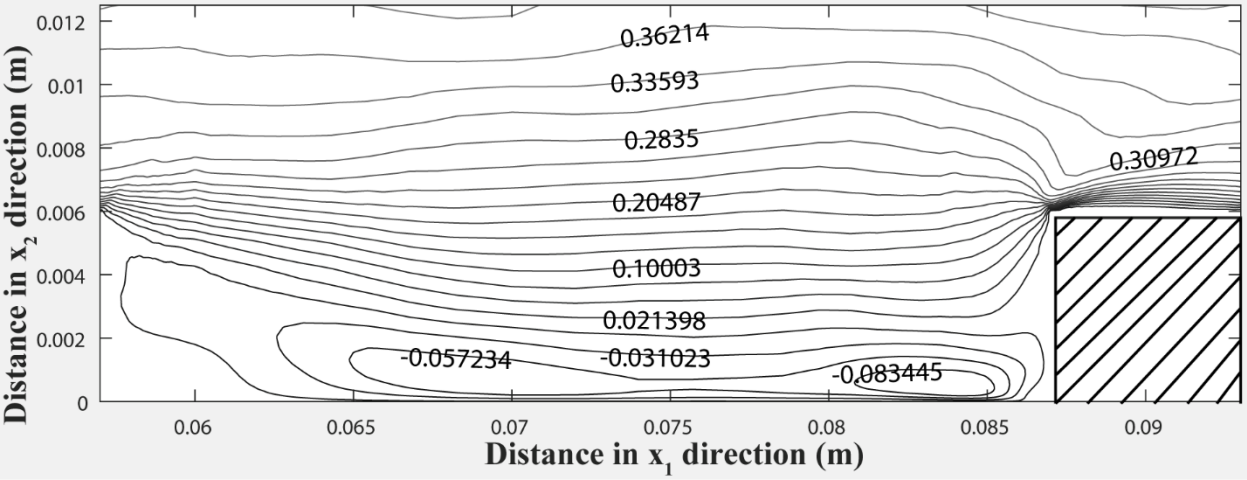

Figure 4-25 Contour of horizontal velocity component for Run 3.

The streamlines of flow for Run 4 (λ/k = 8) are shown in Figure 4-26 the channel section between x_1 = 0. 075 and 0. 1225 m, including the 3rd bar. A large counter-cyclonic eddy appears on the downstream side of a bar, companied by a small cyclonic eddy in the lower corner. Streamlines of the main flow deepen as they pass over the large eddy, come to contact with a portion of the channel floor, and tilt up over a small eddy in the lower right corner.

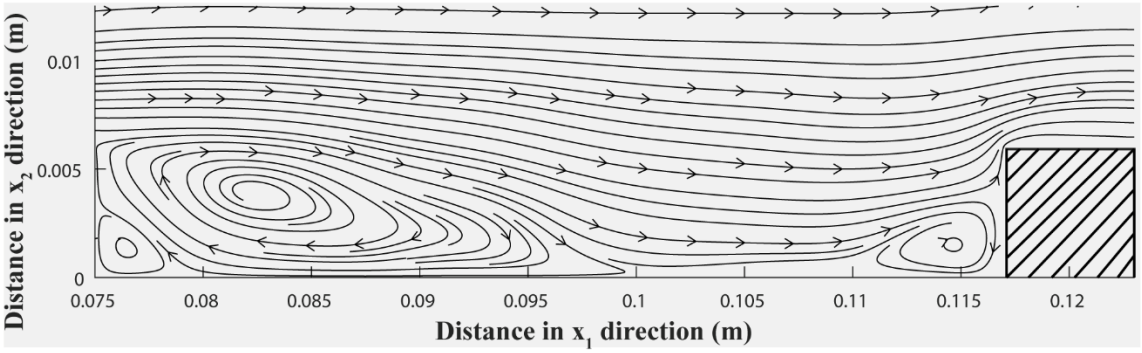

Figure 4-26 Streamlines of flow at the channel centreline for Run 4.

Contours of the horizontal velocity component, U_1, for Run 4 are shown in Figure 4-27 for the same plane as Figure 4-26. The contours have spatial distribution similar to those (Figure 4-25) for Run 3, except the reverse flows in two separate regions near the channel floor. They are respectively located in the two lower corners of the cavity. A slight velocity overshoot is seen on the top of the bar, in response to the large deflective angle when the flow passes the upstream edge of the bar. The shear layer is thicker and wavier for Run 4 than Run 3.

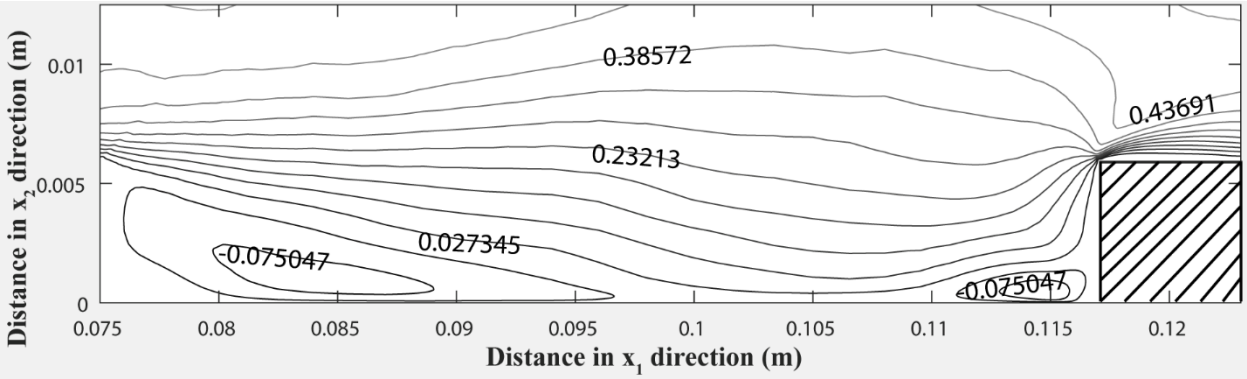

Figure 4-27 Contours of the horizontal velocity component U_1 for Run 4.

The streamlines of flow for Run 5 with staggered cubes at the channel-bed are shown in Figure 4-28. Main flow streamlines come to contact with the entire channel-bed. The flow of water emerges from the upstream edge of the preceding cube (Figures 3-17 and 3-18), and diverges towards downstream. A counter-cyclonic eddy forms in the lower corner on the upstream side of the following cube. The streamlines have patterns different from those for Runs 1 to 4 with transverse bars at the channel-bed.

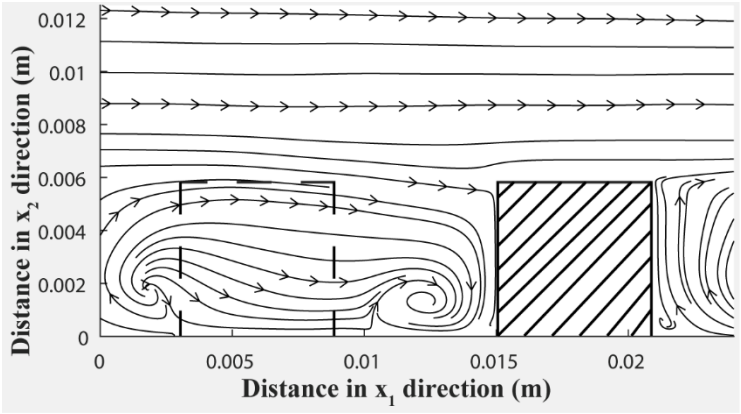

Figure 4-28 Streamlines of flow at the channel centreline for Run 5. The dash lines represent a cube in a plane parallel to the above-mentioned vertical plane.

Contours of the horizontal velocity component, U_1, for Run 5 is shown in Figure 4-29. They show dense spatial distributions along the top of a cube between its upstream and downstream edges (Figures 3-17 and 3-18). From the downstream edge, the contours gradually diverge towards downstream, and then converge towards the upstream edge of the following cube. The velocities are very low in the centre region between adjacent cubes, meaning a partial blockage of flow through the region.

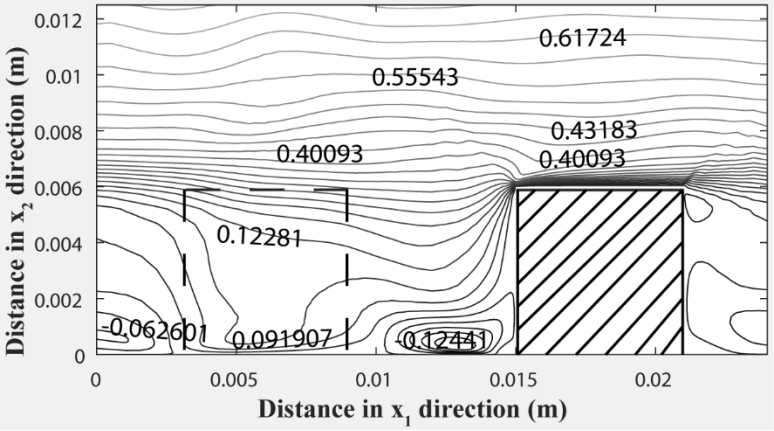

Figure 4-29 Contours of the horizontal velocity component U_1 for Run 5.

4.7 Contour of Turbulence Kinetic Energy

The differences in λ/k for Runs 4 (Tables 3-1 and 3-2), 3, 2 and 1 result in different distributions (Figures 4-30, 4-31, 4-32, 4-33) of the turbulence kinetic energy (TKE), given in Equation [4-6]. In the equation, the overbar denotes the time-average of the quantity in question over a six-second period, which is similar to Equation [4-4]. When $\lambda/k = 8$ (Figure 4-30), high TKE values occur at the downstream edge ($0.12\ m < x_1 < 0.123\ m$, $x_2 = 0.006\ m$) of the bar′s top surface, along the upper half ($x_1 = 0.117\ m$, $0.003\ m < x_2 < 0.006\ m$) of the bar′s upstream surface (Figures 3-15 and 3-16), and above separation regions ($x_1 = 0.095\ m$, $x_2 = 0.01\ m$). TKE originates from the top surface ($0.12\ m < x_1 < 0.125\ m$, $x_2 = 0.006\ m$). It is transmitted downstream and dispersed into the mainstream. This is due to the shear layer that originates from the top surface and develops above

the separation region off the downstream surface of the bar.

$$k = \frac{1}{2}(\overline{(u_1')^2} + \overline{(u_2')^2} + \overline{(u_3')^2}) \qquad [4\text{-}6]$$

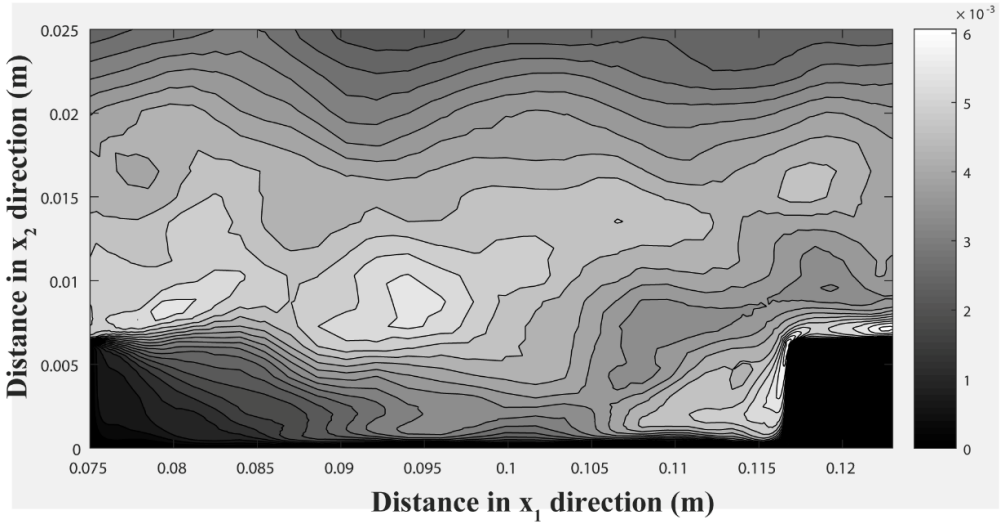

Figure 4-30 Contours of the turbulence kinetic energy in the vertical plane at the channel centreline (or $x_3 = 0.0375$ m) for Run 4.

When $\lambda/k = 6$ (Figure 4-31), high TKE values occur along the upper part of the upstream surface ($x_1 = 0.0875$ m, $0.003\text{ m} < x_2 < 0.006$ m) and the upstream half of the top surface ($0.0875\text{ m} < x_1 < 0.09$ m, $x_2 = 0.006$ m), as well as just upstream ($x_1 = 0.08$ m, $x_2 = 0.008$ m) of the separation region. A new region of high TKE values appears upstream of the bar, around ($x_1 = 0.082$ m, $x_2 = 0.007$ m).

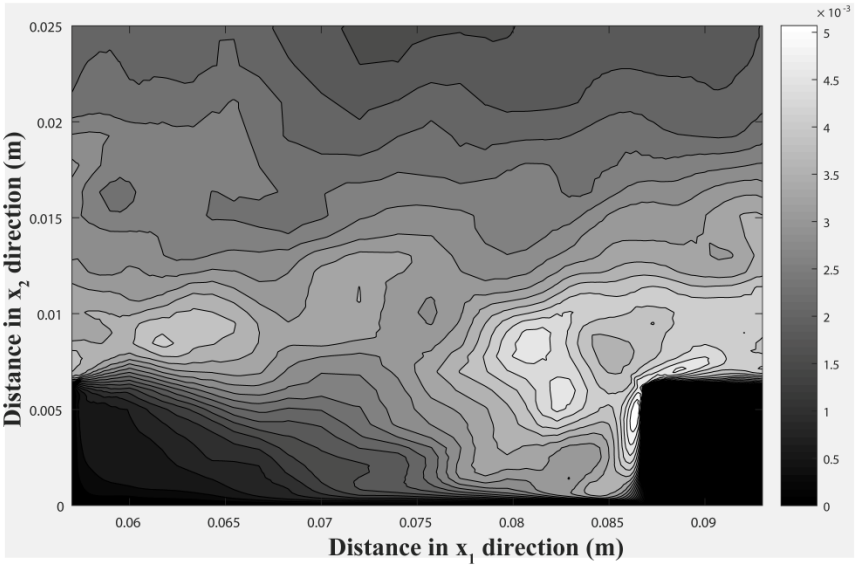

Figure 4-31 Contours of the turbulence kinetic energy in the vertical plane at the channel centreline for Run 3.

When λ/k = 4 (Figure 4-32), contours of TKE have distribution patterns similar to those in Figure 4-31, where λ/k = 6, but show more regions of high TKE values above the bar bar top in the mainstream. Thus, the bed roughness affects the mainstream region to a larger extent when λ/k is equal to four than six.

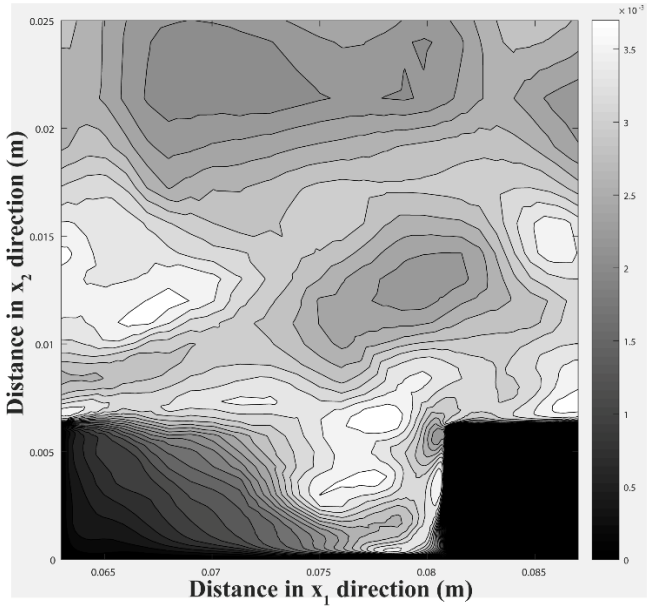

Figure 4-32 Contours of the turbulence kinetic energy in the vertical plane at the channel

centreline for Run 2.

When λ/k = 2 (Figure 4-33), the TKE values are low in the cavity. They increase rapidly over a short vertical distance above the roughness height. The highest TKE value is $1.3x10^{-3}$ (m^2/s^2), occurring near the downstream end of the bar's top surface (x_1 = 0.082 m, x_2 = 0.006 m). The locus (the dashed curve) of the local maxima of TKE appears as a sinusoid that has the highest value at the downstream edge (x_1 = 0.081 m, x_2 = 0.006 m) of the bar and the lowest value at the upstream edge (x_1 = 0.075 m, x_2 = 0.006 m) of the bar. The dashed curve overlaps with the trace of the shear layer where velocity gradients are significant. Starting from the upstream edge of the bar's top surface (x_1 = 0.075 m, x_2 = 0.006 m), the shear layer produces TKE. The energy propagates and diffuses through two paths: a) The dashed curve extends beyond the point of the maximum TKE, which represents one of the paths for the TKE to propagate and diffuse along the mainstream; b) The other path is the penetration of significant TKE gradients into the cavity. Along this path, the penetration interacts with the eddy generated inside the cavity, intensifies when it approaches the bar′s upstream surface (x_1 = 0.075 m, 0 m < x_2 < 0.006 m), and then diffuses into the eddy centre and near-bed region.

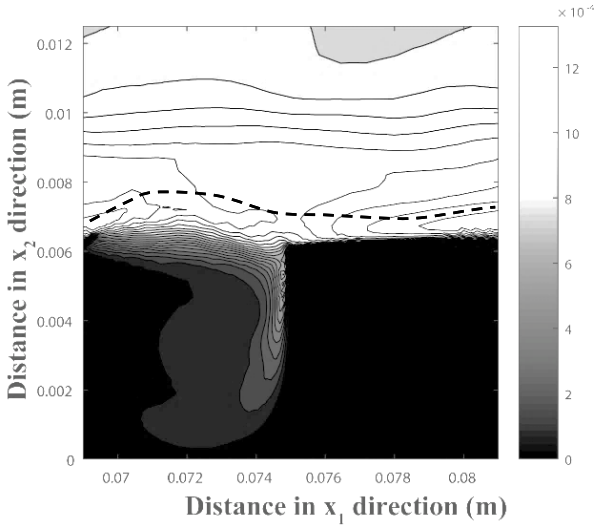

Figure 4-33 Contours of the turbulence kinetic energy in the vertical plane at the channel centreline for Run 1

Figure 4-34 shows the TKE contours for Run 5. A source region of high TKE values appears upstream (x_1 = 0.006 m, x_2 = 0.007 m) of the preceding staggered cube. It is possible that the shear

layer on the side surface (0.003 m < x_1 < 0.009 m, 0 m < x_2 < 0.006 m, x_3 = 0.0405 or 0.0345 m) of the upstream cube (Figures 3-17 and 3-18) produces TKE and enhances the source region. A region of low TKE appears in the lower half (0.003 m < x_1 < 0.009 m, 0 m < x_2 < 0.003 m) of the upstream cube, where both TKE and velocities are low. Similar to Run 1 (λ/k = 2) to 4, Run 5 predicts some regions of high TKE above the roughness height (x_1 = 0.006 m, x_2 = 0.0075 m). A region of high TKE forms above the downstream end (x_1 = 0.006 m, x_2 = 0.021 m) of the cube.

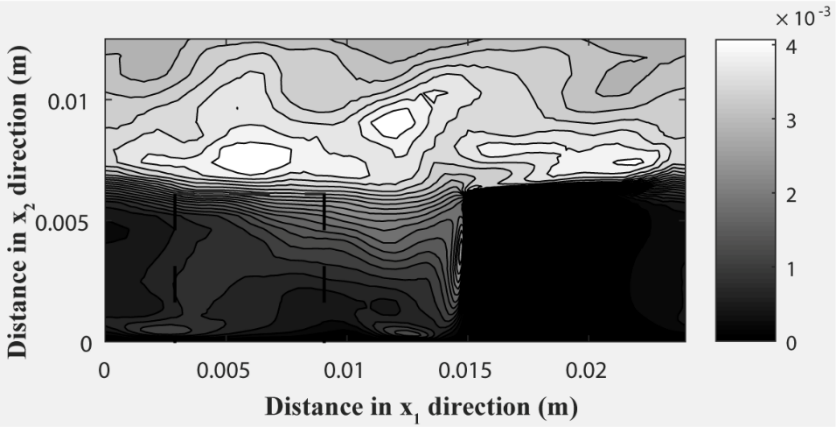

Figure 4-34 Contours of the turbulence kinetic energy in the vertical plane at the channel centreline for Run 5. The dash lines represent a cube in a plane parallel to the above-mentioned plane.

4.8 Power Spectral Density (PSD)

Power spectral density E(κ) is useful for investigating the distribution of flow energy associated with eddies of different sizes. E(κ) is defined as (Pope 2001, p. 78):

$$E(\kappa) = \int_{-\infty}^{\infty} \frac{1}{2} \Phi_{ij}(\kappa) \delta(|\kappa| - \kappa) d\kappa \qquad [4\text{-}7]$$

where δ is the Dirac delta function; $\Phi_{ij}(\kappa)$ is the Fourier transform of two-point covariance, defined as (Pope 2001, p. 77):

$$\Phi_{ij} = F\{R_{ij}(r)\} \qquad [4\text{-}8]$$

where F denotes a Fourier transform. $R_{ij}(r)$ is a two-point covariance, defined as (Pope 2001, p.

77):

$$R_{ij} = < u_i(x_i) u_j(x_i + r) > \quad [4\text{-}9]$$

where < > denotes the mean velocity field, defined as (Pope 2001, p. 74):

$$< U_i(x_i, t) > = \int_{-\infty}^{\infty} \int V_i f(V_i; x_i, t) dV_1 dV_2 \quad [4\text{-}10]$$

where V_i is the sample-space variables corresponding to U_i.

Figures 4-35 and 4-36 shows the PSD calculated for Run 4, using LES data of U_1 and U_2 from the planes having the same dimensions in the x_1- and x_2-direction. The data of the former figure is taken from the plane having the dimension of 0.48 m; the data of the latter one is taken from the plane having the dimension of 0.075 m. Since the calculations of the PSD require data from a plane of equal dimensions in the x_1- and x_2 directions, and thus a rectangle of 0.48 m in the x_1-direction and 0.2025 m in the x_2-direction is attached below and above the LES model channel. The rectangles are filled with values of zero for the velocity components. Figure 4-36 differs from Figure 4-35 in that the former only covers the channel section between the 4th and 6th bars. The lower limit of the wavenumber is smaller in Figure 3-35 than 3-36 because the x_1 dimension of the channel section under investigation is larger in the former than the latter. The Kolmogorov -5/3 law is shown in the figures for comparison.

The PSD curves in both figures show characteristics of energy cascade that are consistent with the results reported in the literature, in particular the energy distribution for the inertia subrange. According to Rodi (2017), the peak value of $E(\kappa)$ is associated with eddies of wavenumber smaller than ten. This feature is not seen from the figures because of the cut-off of eddy sizes. The size of the largest eddy from the LES results appears to fall between the energy-containing eddies and eddies in the inertial subrange.

The sudden decrease in $E(\kappa)$ associated with the smallest eddies (or largest wavenumbers) is due to motion scales smaller than the filter width Δ, where $\Delta = (\Delta_1 \Delta_2 \Delta_3)^{1/3}$. These small eddies are not accommodated by the LES mesh used. For Runs 1 to 3 and 5, the PDS curves (not shown) are very similar to those (Figures 4-35 and 36) for Run 4.

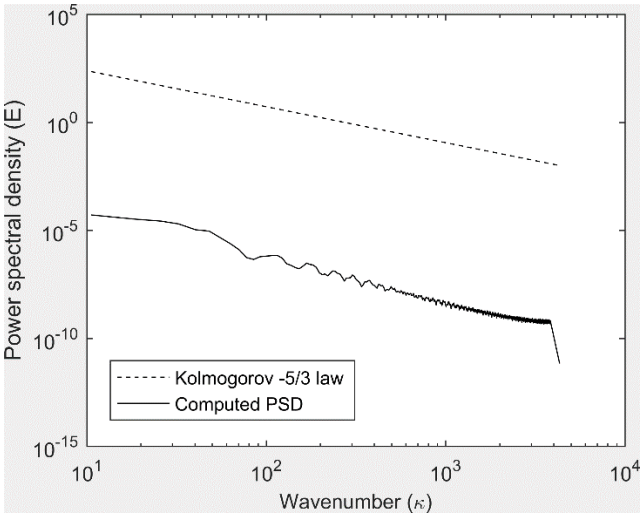

Figure 4-35 PSD calculated for Run 4. The data of U_1 and U_2 as input to the calculations are from the plane at the channel centreline (or $x_3 = 0.0375$ m) between $x_1 = 0$ and 0.48 m (or the entire length of the model channel, see Figure 3-9)

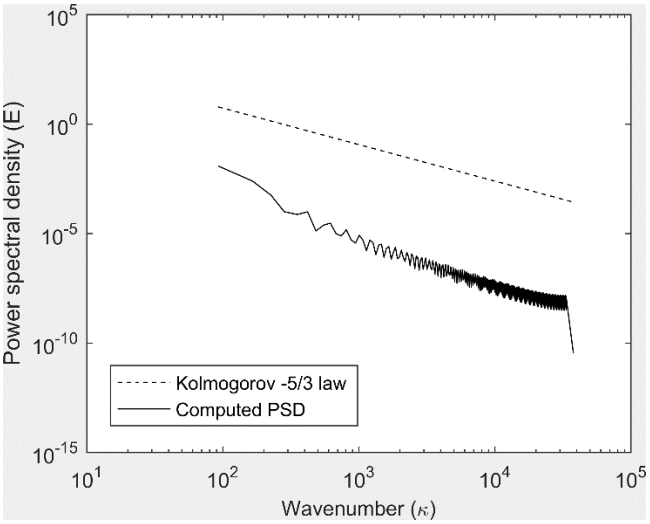

Figure 4-36 PSD calculated for Run 4. The data of U_1 and U_2 are from the plane at the channel centreline between $x_1 = 0.168$ and 0.264 m (or the channel section between the 4th and 6th bars, see Figure 3-9)

4.9 Comparison with wind-tunnel experiments

Air flows in wind tunnels show similar flow characteristics as water flows in flumes. The Reynolds number, and Froude number are the two major parameters for discussions of the similarity between wind tunnel and flume experiments. In terms of the Reynolds number, inertial forces and viscous forces are considered as the major factors determining the flow motions in both experiments. In terms of the Froude number, inertial forces and gravitational forces are considered as the determining factors. Because wind tunnels usually do not have free surface, the Froude number is not considered. This is different from open channel flow experiments.

One can expect that wind tunnel experiments provide similar flow characteristics as water flume experiments when both experiments have the same Reynolds number. To the best of our knowledge, all of the wind tunnel experiments of flow over repeated bars are conducted at the Reynolds numbers (based on roughness height and free stream velocity) in the range of 10000-50000 (Okamoto et al., 1993; Liou et al., 1993; Casarsa and Arts, 2002; Rau et al, 1998). This study uses water-flume experimental data at the Reynolds number of 2400 (based on roughness height and free stream velocity). In this section, two vertical profiles of horizontal velocity from LES of this study are compared with wind-tunnel experimental data from Okamoto et al. (1993), who conducted the experiments at the Reynolds number of 10000 (based on roughness height and free stream velocity).

Figure 4-37 compares the mean streamwise velocity profile at the 7^{th} bar centre for Run 1 (λ/k = 2, d-type roughness flow, Tables 3-1 and 3-2), with the wind-tunnel data and water-flume experimental data. The velocity profile is representative because of the nearly identical flow characteristics at each corresponding bar section. The wind tunnel measurements (the asterisk symbols) match the water flume measurements (the plus symbols) very well, the maximum differences falling within 7%.

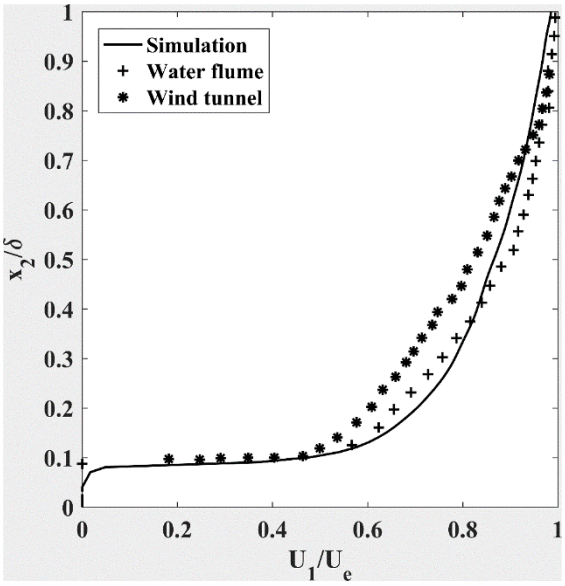

Figure 4-37 A comparison of the mean streamwise velocity profiles (U_1/U_e) for Run 1 (solid curve), with the wind tunnel data (asterisk symbol), and water flume data (plus symbol). δ denotes the boundary layer thickness.

Figure 4-38 compares the mean streamwise velocity profile at the centre of the 6th bar for Run 4 (λ/k = 4, k-type roughness flow, Tables 3-1 and 3-2), with wind tunnel data and water flume data. The wind tunnel data (asterisk symbols) matches the water flume data (plus symbols) with relatively large difference (up to 25%).

Both the water and wind velocity profiles are sensitive to bed roughness configurations. Between Figure 4-37 and 4-38, the water velocity profiles appear to be more sensitive. The wind tunnel experimental results are closer to the water flume experimental results for d-type roughness than k-type roughness.

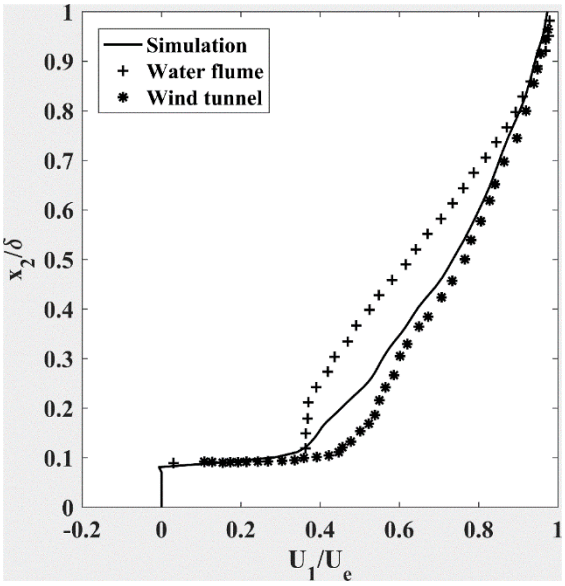

Figure 4-38 A comparison of the mean streamwise velocity profile (U_1/U_e) for Run 4 (solid curve), with wind tunnel data (asterisk symbol), and water flume data (plus symbol).

4.10 Highlights of Contributions

Rough surface flow is an important topic in hydraulic engineering. Significant contributions from this numerical study of the topic are highlighted below:

1. This study simulates turbulent flows over square bars and cubes in shallow open-channels, which is new. Previous numerical studies of the topic have focused on rough surface flow in deep channels. The roughness elements have more profound effects on the flow in shallow than deep channels.

2. This study has recognised the importance of properly treating channel sidewalls, and associated secondary flow, for accurate simulations of rough surface flow. Previous numerical studies of the topic tried to modify the conditions applied at the lateral open boundaries in the streamwise direction, in an attempt to improve shear stress predictions.

3. This study has found a novel resolution to model channel discretisation that can effectively accommodate flow boundary layer next to rough element surfaces, eddy motions in the cavity

between adjacent elements, and external flow structures overlying the cavity. This is without increasing the overall computing costs.

4. This study allows for the use of longer channels than previous numerical studies of rough surface flows. The accuracy uncertainty is smaller when large eddy simulations use longer channels.

5. This study has contributed to an improved understanding of the characteristics of flow over three-dimensional cubes and two-dimensional bars in open channels.

6. This study investigates the power spectral density for the flows over regularly placed bars and staggered cubes. The PSD curves for all the runs show characteristics of energy cascade that are consistent with the results reported in the literature (Rodi, 2017), in particular the energy distribution for the inertia subrange.

Chapter 5
Conclusions

This thesis reports large eddy simulations of turbulent flows in shallow open channels with a rough bed. The rough surface was created in two different configurations: 1) by placing transverse square bars, and 2) by placing cubes, at a flat channel-bed. In the first configuration, the pitch ratio, λ/k, is given values of 2 (or d-type roughness flow), 4, 6, and 8 (or k-type roughness flow) (Tables 3-1 and 3-2). In the second configuration, the cubes are staggered, covering one-fourth of the total bed area. The simulations produce results of flow velocity profiles, time series of flow velocities, streamlines, and contours of flow velocities, power spectral densities, turbulence intensities, and Reynolds shear stresses.

The results of the d-type and k-type roughness flows are compared with available experimental data of Tachie & Adane (2007). The results of streamwise velocity (Equation [4-1]) profiles match the data very well: the maximum discrepancy is below 5% (Figure 4-6) for the d-type roughness flow, and 10% (Figure 4-9) for the k-type roughness flow. The discrepancies are relatively large for the vertical velocity for both the d-type and k-type roughness flows (Figures 4-8 and 4-11). At different depths, the vertical velocities from the simulations appear to fluctuate around zero, but the experimental data show significant upward flow velocity in the middle depth region (or x_2/H = 0.5).

With regard to the streamwise turbulence intensity (Equation [4-2]), the simulations match the experiments very well. Between them, the maximum discrepancy of intensity is lower than 15% for both the d-type (Figure 4-12) and k-type (Figure 4-13) roughness flows. For the d-type flow, the intensity is slightly under-predicted for the lower water column (at x_2/H = 0.2). For the k-type flow, the intensity is slightly over-predicted in the depth range of x_2/H = 0.2 to 0.4.

For the d-type roughness flow (Figure 4-14), the simulation results show two peak values for the vertical turbulence intensity (Equation [4-2]), which occur in the water column at x_2/H = 0.2 and 0.6, respectively. The intensity drops to zero at the water surface. The occurrence of a peak value at x_2/H = 0.2 is consistent with the experiments. For the k-type roughness flow (Figure 4-15), the vertical turbulence intensity is generally over-predicted except near the water surface. For example, at the depth of x_2/H = 0.3, the peak intensity is over-predicted by 17%. At the water surface, the

simulations give negligible values for the vertical turbulence intensity, whereas the experiments give a value of 0.035.

In terms of the Reynolds shear stress (Equation [4-4]) for the d-type roughness flow (Figure 4-14), the simulations reproduce the experiments for the lower one-third of the total water column. In the upper two-thirds of it, the experimental data shows that the shear stress drops to 0.2×10^{-3} (m^2/s^2) at the depth of $x_2/H = 0.6$ and remains constant further up. In comparison, the simulations give shear stresses fluctuating around 1.5×10^{-3} (m^2/s^2) in the depth range of $x_2/H = 0.1$ to 0.6, and dropping to zero at the water surface. For the k-type roughness flow (Figure 4-17), the simulations produce Reynolds shear stresses close to the measured values, for the lower one-tenth of the total water column. The simulations give the correct depth where the peak shear stress occurs but over-predict shear stress magnitudes, when compared to the experiments.

Overall, the simulations produce velocity profiles of good quality, and streamwise turbulence intensities of acceptable accuracy. Nevertheless, the errors are relatively large in the simulation results of vertical turbulence intensity, and Reynolds shear stress. It seems that the large eddy simulations have produced accurate flow characteristics in the streamwise direction, but less accurate results in the vertical direction. A plausible reason is the side wall effects. It is challenging to realistically capture secondary flow that creates transverse vortices in the transverse direction on both sides of the channel. These vortices cause upward motions in the middle of the channel.

The simulations produce a variety of flow patterns in the cavity between two adjacent bars. A common feature of the patterns is the existence of three eddies: one large, strong, anti-cyclonic eddy that dominates the cavity; one small, weak, cyclonic eddy in each of the two lower corners of the cavity. At a pitch ratio of $\lambda/k = 2$ (Figure 4-20), the anti-cyclonic eddy occupies almost the entire cavity, and fluid circulations of the main flow above the bars are virtually isolated from the flow within the cavity.

At $\lambda/k = 4$ (Figure 4-22), the small eddy in the lower right corner weakens and becomes insignificant. The small eddy in the lower left corner strengthens and grows in size, compared to the case where $\lambda/k = 2$, but it is still much smaller than the large, anti-cyclonic eddy. There are some interactions of fluid circulation between the main flow above the bars and the flow within the cavity.

As the λ/k ratio increases to 6 (Figure 4-24), the main characteristics are that the larger, anti-cyclonic eddy migrates toward upstream, with its centre moving closer to the downstream face of bars. A small eddy forms next to their upstream face. At $\lambda/k = 8$ (Figure 4-26), three eddies form in the cavity, with the largest eddy next to the downstream face of bars, and a small eddy in each of the lower corners of the cavity.

Clearly, the flow patterns and velocity field are sensitive to the λ/k ratio. At $\lambda/k = 2$ (Figure 4-21), the flow velocity evenly and gradually increases from the top of bars to the free surface. At $\lambda/k = 4$ (Figure 4-23), eddy motions give rise to a region of reverse flow in the lower half of the cavity, and the velocity contours converge next to the upstream edge of the top of bars, meaning higher shear stresses, compared to the case where $\lambda/k = 2$. At $\lambda/k = 6$ (Figure 4-25), the region of reverse flow appears to shrink. At $\lambda/k = 8$ (Figure 4-27), the region of reverse flow further shrinks, and the shear stress at the upstream edge of the top of bars further intensifies. Thus, an increase in λ/k causes a decrease in the region of reverse flow and higher shear stress on the upstream edge of bars. In the case of staggered cubes (Figure 4-29), they create restrictions on reverse flow, and enhance the shear stress at the upstream edge of cubes.

The PSD curves for all the runs (Tables 4-35 and 4-36) show characteristics of energy cascade that are consistent with the results reported in the literature, in particular the energy distribution for the inertia subrange. According to Rodi (2017), the peak value of $E(\kappa)$ is associated with eddies of wavenumber smaller than ten. This feature is not seen from the figures because of the cut-off of eddy sizes. The size of the largest eddy from the LES results appears to fall between the energy-containing eddies and eddies in the inertial subrange. The sudden decrease in $E(\kappa)$ associated with the smallest eddies (or largest wavenumbers) is due to motion scales smaller than the filter width Δ, where $\Delta = (\Delta_1 \Delta_2 \Delta_3)^{1/3}$. These small eddies are not accommodated by the LES mesh used.

Many researchers have chosen to use the "velocity inlet" and "pressure outlet" boundary conditions in their numerical studies of open-channel flows based on the Reynolds-averaged Navier-Stokes equations. It is shown in this thesis that such choice is not desirable in large eddy simulations. The reason is that a relative long entrance length must be included as part of the model channel in order to reach a fully developed flow, and as a result, the computing costs become prohibitively high. The present study proves that cyclic boundary conditions can be applied in both the streamwise and transverse directions for simulations of fully developed flow. On the one hand, the application

of the conditions enhances computation efficiency. On the other hand, it eliminates the effects of artificial sidewalls and thus improves the accuracy of mean velocity and turbulence intensity predictions.

Chapter 6
Suggestions for Future Work

It would be interesting to extend the present study by considering the following points in future investigations:

1. Explore large eddy simulation (LES) strategies to improve the results of turbulence intensities and the Reynolds shear stresses. These quantities are of engineering relevance. Extend the time period of simulations to perhaps 180 s for time-averaged quantities from LES results. Due to limited data-storage capacity and computing power in the current study, the time period was 6 s, compared to 120 s of measurements in experiments.

2. Investigate frictional effects, turbulence kinetic energies, event frequencies, and streaky structures, in addition to velocity profiles, turbulence intensities, and Reynolds shear stresses as discussed in the current study.

3. Systematically assess the suitability of rigid-lid conditions applied at the top boundary (water surface) of a shallow water channel. It is unclear to what extent the the bottom-boundary layer interacts with the top boundary. Systematically evaluate the suitability of cyclic conditions implemented at the flow inlet and outlet. The current study has demonstrated some advantages of the conditions. However, how and to what extent this implementation affects the simulation results are still unknown.

4. Pursue LES of high Reynolds number flows in shallow open-channels, and validate the computational results using measurements from the near-bed region. To the best of our knowledge, currently such measurements have not been reported in the pre-existing literature. In addition, the measurments from existing laboratory experiments of rough-surface flow suffer artifical sidewall effects, causing uncertainties in data comparisons between computer simulations and laboratory experiments.

5. Ideally, the filter widths in LES should be the same in all of the three dimensions. However, this requirement is difficult to achieve in practical applications. A number of suggestions for addressing the issue have been reported in the pre-existing literature (Gerasimov, 2014).

It is worth tackling the issue in future LES studies of shallow water flow.

6. Ideally, the PDS should show the peak of $E(\kappa)$ in energy containing range. According to Rodi (2017), the peak value of $E(\kappa)$ is associated with eddies of wavenumber smaller than ten. This feature is not seen from the figures because of the cut-off of eddy sizes. The size of the largest eddy from the LES results appears to fall between the energy-containing eddies and eddies in the inertial subrange. It is worth creating a larger domain to investigate the whole PDS curve in the future LES studies.

References

Akan, A. O. (2011). *Open channel hydraulics*. Elsevier.

Bagherimiyab, F., & Lemmin, U. (2013). Shear velocity estimates in rough-bed open-channel flow. *Earth Surface Processes and Landforms, 38*(14), 1714-1724.

Casarsa, L., & Arts, T. (2002). Aerodynamic performance investigation of a rib roughened cooling channel flow with high blockage ratio. In *11th International Symposium on Applications of Laser Techniques to Fluid Mechanics, Lisbon, Portugal*.

Cheng, H., Hayden, P., Robins, A., & Castro, I. (2007). Flow over cube arrays of different packing densities. *Journal of Wind Engineering and Industrial Aerodynamics, 95*(8), 715-740.

Choi, H., & Moin, P. (2012). Grid-point requirements for large eddy simulation: Chapman's estimates revisited. *Physics of fluids*, *24*(1), 011702.

Chow, V. (1959). *Open channel hydraulics* McGraw-Hill Book Company, Inc; New York.

Coceal, O., Dobre, A., Thomas, T., & Belcher, S. (2007). Structure of turbulent flow over regular arrays of cubical roughness. *Journal of Fluid Mechanics, 589*, 375-409.

Cui, J., Patel, V. C., & Lin, C. (2003). Large-eddy simulation of turbulent flow in a channel with rib roughness. *International Journal of Heat and Fluid Flow, 24*(3), 372-388.

Djenidi, L., Elavarasan, R., & Antonia, R. (1999). The turbulent boundary layer over transverse square cavities. *Journal of Fluid Mechanics, 395*, 271-294.

Dritselis, C. (2014). Large eddy simulation of turbulent channel flow with transverse roughness elements on one wall. *International Journal of Heat and Fluid Flow, 50*, 225-239.

Flack, K. A., Schultz, M. P., & Shapiro, T. A. (2005). Experimental support for Townsend's Reynolds number similarity hypothesis on rough walls. *Physics of Fluids, 17*(3), 035102.

Fluent, A. (2013). ANSYS fluent theory guide 15.0. *Inc, Canonsburg, PA,*

Gerasimov, A. (2014). Quick Guide to Setting Up LES-type Simulations.

Germano, M., Piomelli, U., Moin, P., & Cabot, W. H. (1991). A dynamic subgrid-scale eddy viscosity model. *Physics of Fluids A: Fluid Dynamics, 3*(7), 1760-1765.

Giannopapa, C., & Papadakis, G. (2007). Indicative Results and Progress on the Development of the Unified Single Solutions Method for Fluid-Structure Interaction Problems. Paper presented at the *Proceedings 2007 ASME Pressure Vessels and Piping Division Conference, San Antonio, Texas, July,* 22-26.

Lacey, R. J., & Rennie, C. D. (2011). Laboratory investigation of turbulent flow structure around a bed-mounted cube at multiple flow stages. *Journal of Hydraulic Engineering, 138*(1), 71-84.

Leonardi, S., Orlandi, P., & Antonia, R. A. (2007). Properties of d-and k-type roughness in a turbulent channel flow. *Physics of Fluids, 19*(12), 125101.

Lilly, D. K. (1992). A proposed modification of the Germano subgrid-scale closure method. *Physics of Fluids A: Fluid Dynamics, 4*(3), 633-635.

Liou, T. M., Hwang, J. J., & Chen, S. H. (1993). Simulation and measurement of enhanced turbulent heat transfer in a channel with periodic ribs on one principal wall. *International Journal of Heat and Mass Transfer*, *36*(2), 507-517.

Miyake, Y., Tsujimoto, K., & Agata, Y. (2000). A DNS of a turbulent flow in a rough-wall channel using roughness elements model. *JSME International Journal Series B Fluids and Thermal Engineering, 43*(2), 233-242.

Moody, L. F. (1944). Friction factors for pipe flow. *Trans Asme, 66*, 671-684.

Okamoto, S., Seo, S., Nakaso, K., & Kawai, I. (1993). Turbulent shear flow and heat transfer over the repeated two-dimensional square ribs on ground plane. *Journal of Fluids Engineering, 115*(4), 631-637.

Perry, A. E., Schofield, W. H., & Joubert, P. N. (1969). Rough wall turbulent boundary layers. *Journal of Fluid Mechanics, 37*(2), 383-413.

Pope, S. B. (2001). *Turbulent Flows* Cambridge University Press.

Rau G., Cakan M., Moeller D., Arts T. (1998). The effect of periodic ribs on the local aerodynamic and heat transfer performance of a straight cooling channel. *ASME*, 120, 368–75.

Raupach, M., Antonia, R., & Rajagopalan, S. (1991). Rough-wall turbulent boundary layers. *Appl.Mech.Rev, 44*(1), 1-25.

Raupach, M., Thom, A., & Edwards, I. (1980). A wind-tunnel study of turbulent flow close to regularly arrayed rough surfaces. *Boundary-Layer Meteorology, 18*(4), 373-397.

Rodi, W. (2017). Turbulence Modeling and Simulation in Hydraulics: A Historical Review. *Journal of Hydraulic Engineering*, *143*(5), 03117001.

Rodi, W., Constantinescu, G., & Stoesser, T. (2013). *Large-eddy simulation in hydraulics* Crc Press.

Schlichting, H., Gersten, K., Krause, E., & Oertel, H. (1955). *Boundary-layer theory* Springer.

Tachie, M., & Adane, K. (2007). PIV study of shallow open channel flow over d-and k-type transverse ribs. *Journal of Fluids Engineering, 129*(8), 1058-1072.

Townsend, A. A. (1980). *The structure of turbulent shear flow* Cambridge university press.

Volino, R. J., Schultz, M. P., & Flack, K. A. (2011). Turbulence structure in boundary layers over periodic two-and three-dimensional roughness. *Journal of Fluid Mechanics, 676*, 172-190.

Xie, Z., Lin, B., & Falconer, R. A. (2014). Turbulence characteristics in free-surface flow over two-dimensional dunes. *Journal of Hydro-Environment Research, 8*(3), 200-209.